

**FLUORESCENCE AND ABSORPTION
MEASUREMENTS OF EUROPIUM
DOPED ALUMINO-SILICATE
GLASSES**

By

ABDUR RAHMAN

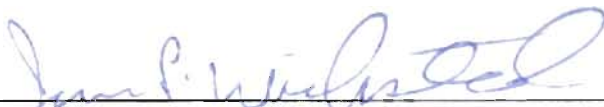
**Master of Science
Dhaka University
Dhaka, Bangladesh
1996**

**Bachelor of Science
Dhaka University
Dhaka, Bangladesh
1994**

**Submitted to the Faculty of the
Graduate College of the
Oklahoma State University
in partial fulfillment of
the requirements for
The Degree of
MASTER OF SCIENCE
July, 2000**

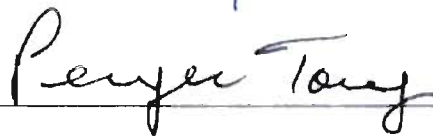
FLUORESCENCE AND ABSORPTION
MEASUREMENTS OF EUROPIUM
DOPED ALUMINO-SILICATE
GLASSES

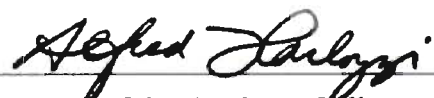
Thesis Approved:



Thesis Advisor







Dean of the Graduate College

ACKNOWLEDGEMENTS

I would like to express my appreciation to my advisor, Dr. James P. Wicksted, for his patience, generosity, and guidance. I also would like to express my gratitude to Dr. George S. Dixon for his valuable discussions. I sincerely appreciate Dr. Abdul Latif Y. Hammad and Dr. Paul Chen for their help with experimental techniques and apparatus.

I would like to thank Dr. Joel Martin and Dr. Aihua Xie for the use of their laboratory equipment.

The financial support of the US Army Research Office was greatly appreciated.

I would like to thank my family and friends for their encouragement as I worked toward my goal.

TABLE OF CONTENTS

Chapter	Page
1. Introduction	1
1.1 History	1
1.2 RE structure and energy levels	3
1.3 Theory	4
2. Experimental setup and procedure	8
2.1 Sample composition and preparation	8
2.2 Density measurement.....	10
2.3 Fluorescence measurements.....	12
2.4 Absorption measurements.....	15
3. Results	17
3.1 Density and Number density.....	17
3.2 Fluorescence results.. ..	18
3.3 Absorption results.....	29
4. Discussion.....	38
4.1 Fluorescence.....	39
4.2 Absorption.....	44
5. Conclusion.....	52
Appendix.....	52
Bibliography.....	57

LIST OF TABLES

Table	Page
2.1-a: Glass sample (Eu ³⁺ Series) constituents in mole percent.....	8
2.1-b : Glass sample (Al series) constituents in mole percent.....	9
2.1-c: Glass sample (Na ⁺ series) constituents in mole percent.....	9
3.1-a: Density and Number density (Eu ³⁺ Series).....	17
3.1-b: Density and Number density (Al Series).....	17
3.1-c: Density and Number density (Na ⁺ Series).....	18
3.1-d: Density and Number density (Sample: OPT).....	18
3.2-a: Integrated intensity ratio(Eu ³⁺ Series): Region-I (20 ⁰ C).....	20
3.2-b: Integrated intensity ratio(Eu ³⁺ Series): Region-I (-35 ⁰ C).....	21
3.2-c: Integrated intensity ratio(Al Series): Region-I (20 ⁰ C).....	21
3.2-d: Integrated intensity ratio(Al Series): Region-I (-35 ⁰ C).....	21
3.2-e: Integrated intensity ratio(Na ⁺ Series): Region-I (20 ⁰ C).....	22
3.2-f: Integrated intensity ratio(Eu ³⁺ Series): Region-II (20 ⁰ C).....	24
3.2-g: Integrated intensity ratio(Eu ³⁺ Series): Region-II (-35 ⁰ C).....	24
3.2-h: Integrated intensity ratio(Al Series): Region-II (20 ⁰ C).....	24
3.2-i: Integrated intensity ratio(Al Series): Region-II (-35 ⁰ C).....	25
3.2-j: Integrated intensity ratio(Na ⁺ Series): Region-II (20 ⁰ C).....	25
3.2-k: Integrated intensity ratio(Eu ³⁺ Series): Region-II (20 ⁰ C).....	25

Table	Page
3.2-l: Integrated intensity ratio (Eu ³⁺ Series): Region-II (-35 ⁰ C).....	26
3.2-m: Integrated intensity ratio (Al Series): Region-II (20 ⁰ C).....	26
3.2-n: Integrated intensity ratio (Al ⁺ Series): Region-II (-35 ⁰ C).....	26
3.2-o: Integrated intensity ratio (Na ⁺ Series): Region-II (20 ⁰ C).....	27
3.2-p: Integrated intensity ratio(Sample: OPT).....	27
3.3-a: Judd- Offelt parameters (Eu ³⁺ Series).....	36
3.3-b:Judd- Offelt parameters (Al Series).....	36
3.3-c: Judd- Offelt parameters (Na ⁺ Series).....	36
3.3-d: Judd- Offelt parameters (Sample: OPT).....	37

LIST OF FIGURES

Figure	Page
Figure-1: Two dimensional view of alumino-silicate glass samples	11
Figure-2: Experimental setup for fluorescence transition measurements.....	13
Figure-3: Eu^{3+} energy level diagram.....	14
Figure-4: Fluorescence transitions (Region-I, Sample: 1.5 mole% of Eu^{3+}).....	19
Figure-5: Fluorescence transitions (Region-II, Sample: 1.5 mole% of Eu^{3+}).....	23
Figure-6: Fluorescence transitions (Region-II, Sample: OPT).....	28
Figure-7: Absorption transitions (Al series).....	31
Figure-8: ${}^7\text{F}_0 \rightarrow {}^5\text{D}_2$ Absorption transitions (Al Series).....	32
Figure-9: ${}^7\text{F}_0 \rightarrow {}^5\text{D}_4$ Absorption transitions (Na^+ Series).....	33
Figure-10: ${}^7\text{F}_0 \rightarrow {}^5\text{L}_6$ Absorption transitions (Eu^{3+} Series).....	34
Figure-11: ${}^7\text{F}_0 \rightarrow {}^5\text{L}_6$ Absorption X-section (7.5 mole% of Eu^{3+}).....	35

INTRODUCTION:

Rare earth materials show sharp absorption and emission transition lines while doped within crystals. This interesting feature attracted many physicists during the first half of the 20th century. Besides theoretical approach, application aspects resulted in increased research interest on rare earth doped crystals and rare earth doped glasses as well. Though the transition lines in rare earth (RE) doped glasses are not as sharp as those of rare earth doped crystals, technological needs, along with easy manufacturing, continue to drive research interests in this field. Many techniques such as X-ray, neutron and phonon spectroscopy, Fluorescence Line Narrowing (FLN), absorption and fluorescence technique have been employed via RE energy levels to determine many different glass structures with different rare earth probes. Among all the rare earth materials, Eu^{3+} ion is the most popular microscopic probe for the analysis of rare earth doped solids.

1.1 History

In solids and liquids there are resonance interactions among atoms, mainly with their neighboring ones. In addition, in a solid or liquid, the average thermal motion distance varies among its components, again causing overlapping of energy levels that contributes to line broadening. All these factors give rise to line broadening and even a continuous spectrum. In contrast to all these factors, rare earth ions do show sharp transition lines while incorporated in crystals. J. Becquerel^[1] was the first to observe spectra from rare earth compounds. His research showed that some of the rare earth compounds do exhibit sharp absorption lines. In addition, when doped in crystals, RE absorption lines show considerable Zeeman splitting. The observed spectral line width was found to have nearly the same sharp character as those of gases.

Rare earth's [RE] were scarce and very difficult to obtain in pure form prior to World War II. J. Becquerel's^[1] discovery gave a new dimension to the field of solid state physics because information of the binding of rare earth ions in the solid state provided information about inter-atomic forces. These sharp lines imply that rare earth ions are nearly independent of the influence of crystalline environment, and a one-ion model can be employed to determine the RE energy levels. Therefore, absorption and/or emission spectra of rare earth gasses could be used to find the energy levels of RE atoms in solids. Crystal field effects then can be accounted for as a perturbation. Despite these remarkable features, the analysis of rare earth crystals made very little progress during that era because pure rare earth material was scarce.

In the late 1920's theoretical work by ²Bethe and Kramers helped in correlating the observed splitting of absorption spectral lines in the electric crystalline field with the symmetry of the field. Van Vleck³, in his paper in 1937, wrote that the absorption lines in the crystalline rare earth originates from forbidden transitions within the 4f shell. Despite the fact that there were limitations on purity of the rare earth crystals, contributions from Bethe^[2], Kramers^[2], Joos^[2], Tomschek^[2], Van Vleck^[3] and many others during the 1930's helped in the understanding of the observed phenomenon. After World War II, research accelerated because rare earth elements with high purity and huge amount became available to focus research on rare earth salts. Immediately after the war, Hellwege and his collaborators pioneered the interest in this activity, and Jorgensen and his group at Oxford continued working on corresponding theoretical approach. Dieke and his coworker's^[4] at Johns Hopkins published a complete set of energy levels for all the trivalent rare earth ions in the anhydrous trichlorides during early 1960's.

During the 1960's² a new theoretical approach (Elliot, Stevens, Pryce, Judd, Runciman, etc.) was used which concentrated on details of the electric field splitting and the magnetic behavior derived from the general theory of complex spectra and the interaction of the spins within an external magnetic field.

More than a half century of extensive work brings us to the current period with many potential applications of rare earth metals.

1.2 RE Structure and Energy Levels:

Elements with atomic numbers lying 58-71 are called as lanthanides, often referred as rare earth atoms. $[1s^2 2s^2 2p^6 3d^{10} 4s^2 4p^6 4d^{10} 5s^2 5p^6 5d 6s^2] + 4f^N$ are the well-know neutral lanthanide configurations. A potential well develops in the beginning of the lanthanide series. This draws the 4f electrons to the interior of atom. With the progressive increasing of the atomic number in the series, the entire $4f^N$ shell radii decrease (lanthanide contraction) due to imperfect screening among the 4f electrons^[5]. The 4f eigenfunctions lie inside the $5s^2 6p^6$ closed shells of the xenon structure. As a result, f-eigenfunctions cannot appreciably interact with the environment.

Absorption data had been used to determine energy levels of rare earth doped crystals. Not all crystals gave sharp spectral lines, and low temperature measurements were required. At very low temperatures, the lattice vibration contribution to the line broadening is minimized. Most importantly, there are lower levels that are closely spaced, distributed according to Boltzman law: $\exp(-E_n/K_B T)$. Absorption from these levels may overlap and contribute to line broadening. However, if the temperature is sufficiently low, this overlap does not occur. This theory is applicable to fluorescence as well. At very low temperature the energy (or wavelengths) of the absorption lines can be

used to obtain excited state energy levels relative to the ground state energy levels without any complexity.

Fluorescence spectrum gives low-lying levels. Emission from a single excited state of energy E_0 with a frequency ν will give a low lying level $E_0 = E_0 - h\nu$. The simultaneous emission of different excited states to a lower level helps determine the lower level energy through different fluorescent lines^[2]. In some cases, for allowed absorption lines, some weak absorption lines cannot be found even at very low temperature. Fluorescence in some cases helps to find those levels.

1.3 Theory:

Optical transitions in rare earth ions are of electric dipole, electric quadrupole and magnetic dipole nature. Magnetic dipole and electrical quadrupole transitions are allowed transitions, while electric dipole transitions are forbidden transitions since intra f-f transitions are not parity allowed. These forbidden transitions or the forced electric dipole transitions are accomplished by the mixing of states of opposite parity into these states, which is accomplished by the odd parity terms of the expansion of the crystal field potential. Excited configurations of $4f^N$ configuration can be $4f^{N-1}n'l'$ where $n'l'$ corresponds to 5d or 5g.

Judd^[6] and Offelt^[7] independently concentrated on these transitions. B. R. Judd^[6] wrote about the difficulty in estimating the intensities of electric dipole transitions arises from the admixture $4f^N$ wavefunctions of opposite parity. To calculate such admixtures, not only must the energies and eigenfunctions of configurations, such as $4f^{N-1}5d$ be known but also that part of the crystal field potential responsible for the admixing must be known.

In the works of Judd^[6], the excited configurations are independent of all quantum numbers except n and l ; that is, the excited state configurations are completely degenerate with single energy levels. Moreover, he took the difference of the energy denominators of the initial and final states to be the same, which necessarily are not always close enough to be considered equal. Surely, this assumption makes things much simpler to handle, and these simplifications leads to three parameters ($\Omega_2, \Omega_4, \Omega_6$) called Judd-Offelt^[6,7] intensity parameters. With only these parameters, information on fluorescence and absorption transitions and hence structure of the solids can be understood.

Fluorescence and absorption spectra of RE's drew attention in elucidating not only crystal structure but also glass structure. Glass being an amorphous material does not show long range order. Fluorescence and absorption techniques help in revealing different glass structures when RE's are doped in those glasses. Quite simply, the absorption and emission spectra are not as sharp in glasses as in crystals. Line broadening makes it difficult to extract information of local environments around the RE ions in glass, and it hinders many prospective applications such as glass lasers. Homogeneous and inhomogeneous broadening causes the transition lines to broaden. Homogeneous broadening is due to the average thermal motion of ions in the glass materials. Inhomogeneous broadening has its origin in the overlapping of stark energy levels of different rare earth ions located at different sites and experiencing different ligand fields due to lack of long range order in glass. Low temperature techniques and fluorescence line narrowing technique are two major methods used to encounter this inhomogeneous line broadening.

The Nd^{3+} laser is one important aspect of the application of RE's. For many applications, such as optical devices like optical storage and optical amplifiers, RE's are now investigated, and in some cases are already being employed. These types of applications continue the need for research on the behavior of the homogeneous and inhomogeneous broadening, energy transfer, local glass structure etc..

Calculations of the fluorescence transition ratios and calculations of the Judd-Offelt^[6,7] parameters from absorption and/or fluorescence transitions help in determining ion-sites and their local environment in glass and finally their energy level diagrams.

Crystal field analysis of FLN spectra can provide insight into local structure, while analysis of variations in the spectra as a function of excitation wavelength can provide information in the distribution of sites in glasses. J. R. Morgan et. al^[8] used FLN techniques to investigate homogeneous and inhomogeneous line widths of Eu^{3+} doped borate glasses.

Fluorescence and absorption techniques have been employed on different glasses (borate, silicate, phosphate etc.) incorporated with different RE's. These experiments helped in elucidating the behavior of homogeneous and inhomogeneous transitions of rare earth in glasses and also dealt with energy transfer among the RE ions. In context with the homogeneous broadening, Judd-Offelt^[6,7] parameters also have been calculated from emission absorption data.

Until now, Eu^{3+} has been considered as the most popular microscopic probe in delineating the features of those glasses. This is because

- a) Eu^{3+} has well-resolved stark components and very simple energy levels; and
- b) it possesses a non-degenerated ground (${}^7\text{F}_0$) and excited (${}^5\text{D}_0$) states.

In our experiments, we, therefore, considered Eu^{3+} as our RE ion and doped it into different series of silicate glasses. Absorption and emission spectra of varying concentration of Eu^{3+} , Na^+ and Al have been observed at different temperatures. Ratios of intensities of different fluorescence transitions have been calculated within the same scan. Absorption data at room temperature has been used to calculate Judd-Ofelt^[6,7] parameters. Calculated values from absorption and fluorescence data have been used to explain the compositional dependence of the local environment of the Eu^{3+} ions in these alumino-silicate glasses.

EXPERIMENTAL SETUP AND PROCEDURE:

2.1 Sample Composition and Preparation:

We used different glass samples with varying concentrations of their constituents. The variation of the glass concentration can be considered as three different series. They are as follows:

1. Varying Eu^{3+} concentration (Eu^{3+} series: Table 2.1-a):



$x = 1.5, 2.5, 5.0, 7.5, 10.0, 15.0$ in mole%.

Table 2.1-a: Glass Sample Constituents in mole percent.

Base composition (in mole%)*x%	Base composition (in mole%)*(1-x)%			
$\text{Eu}_2\text{O}_3(x)$	SiO_2	Na_2O	MgO	Al_2O_3
1.5	68.950	14.775	11.820	2.955
2.5	68.250	14.625	11.700	2.925
5.0	66.500	14.250	11.400	2.850
7.5	64.750	13.875	11.100	2.775
10.0	63.000	13.500	10.800	2.700
15.0	59.500	12.750	10.200	2.550

2. Varying Al concentration (Al series: Table 2.1-b):



$x = 0.0, 3.0, 6.0, 9.0$ and 15.0 in mole%.

Table 2.1-b: Glass Sample (Al series) constituents in mole percent.

Base composition (in mole%)*x%	Base composition (in mole%)*(1-x)%			
Eu ₂ O ₃ (x)	SiO ₂	Na ₂ O	MgO	Al ₂ O ₃
2.5	71.175	14.625	11.700	0.0
2.5	65.325	14.625	11.700	5.850
2.5	62.400	14.625	11.700	8.775
2.5	56.550	14.625	11.700	14.625

3. Varying Na⁺ concentration (Na⁺ series: Table 2.1-c):

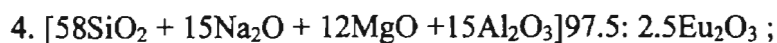


x = 10.0, 15.0, 20.0 and 25.0 in mole %.

Table 2.1-c: Glass Sample (Na⁺ series) constituents in mole percent.

Base composition (in mole%)*x%	Base composition (in mole%)*(1-x)%			
Eu ₂ O ₃ (x)	SiO ₂	Na ₂ O	MgO	Al ₂ O ₃
2.5	73.125	9.750	11.700	2.925
2.5	63.375	19.500	11.700	2.925
2.5	58.500	24.375	11.700	2.925

In addition to all these samples we used another sample (sample: OPT) which has the following composition



Europium carbonate, aluminum hydroxide, alkali carbonate, alkaline earth carbonate and silica precursor powders were mixed according to specific proportions for one hour and placed in a platinum crucible to obtain the glass samples mentioned above. The crucible is placed in a furnace, and the mixture is melted at 1650°C for 8-50 hours. The mixture is then cooled to 1550°C at $-10^{\circ}\text{C}/\text{hour}$ during the melting furnace ramp-down. The crucible and charge were then placed in a separate annealing oven (pre-heated to $450-550^{\circ}\text{C}$) and annealed for 1 hour at $700-725^{\circ}\text{C}$. The annealed glass was removed from the crucible by a core drill. The glass material is then cut into semi-cylindrical and rectangular shapes for experimental measurements. Sample faces are then ground and polished to optical quality using a cerium oxide polishing compound. The Figure-1 shows a two dimensional view of the alumino-silicate glass samples (proposed by Dr. Abdulatif Y.Hamad).

2.2 Density Measurement:

Density measurements were carried out on the samples mentioned in section 2.1 using the buoyancy technique based on Archimedes principle. Archimedes' principle was used to calculate the densities of different glass samples. The mass of the samples was measured in air and in water at 20°C . The balance meter we used had an accuracy of $\pm 0.0001\text{gm}$. Results of the density measurements are tabulated in Table 3.1a-3.1d in Chapter 3.

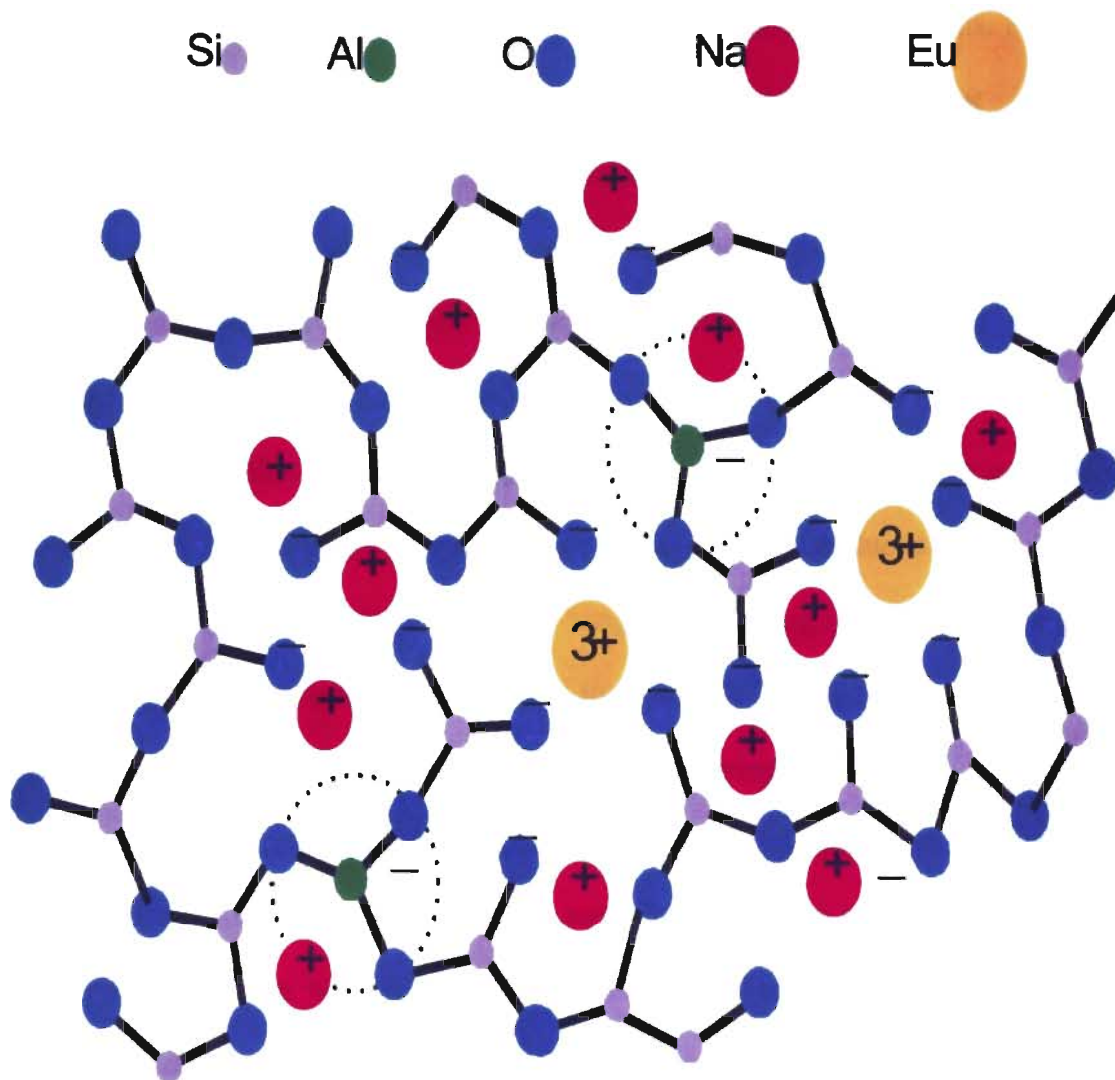


Figure-1: Two dimensional View of Aluminosilicate Glass Samples.
Courtesy: Abdulatif Y. Hamad

2.3 Fluorescence Measurements:

Figure-2 shows the experimental setup for the fluorescence measurements. Fluorescence measurements were done at room temperature (20°C) and at -35°C and at -183°C . For the first two temperatures (20°C , -35°C), the adopted cryostat had four windows made of BK7 glasses. A Melcor thermoelectric cooler was attached to the lid so that it was inside the cryostat during the experiment. Copper plates extended from the cooler were used to hold samples and transfer heat. A heat sink and fan were attached to the outer part of the thermoelectric cooler. Power was supplied to the cooler by a Hewlett Packard 6633A DC power supply and monitored by a Hewlett Packard 3478A multimeter, which read the temperature dependent voltage between Omega Engineering cold junction compensator (ice point) and the copper plates holding the samples. Voltage was then converted to temperature based on data supplied by Omega Engineering.

A second cryostat was employed for the fluorescence and absorption measurements of the samples at -183°C . It had almost the same features as the previous cryostat, but the thermoelectric cooler was replaced by a reservoir attached to the top of the lid. Copper plates, which were used as sample holders, had an extension to the reservoir. Liquid nitrogen was placed in the reservoir to cool the samples to -183°C .

Samples were cleaned with acetone, placed into the cryostat properly so that laser light could be transmitted into the sample unobstructed. Fluorescent light from the rectangular samples was collected by a lens at right angles to the direction of propagation of laser light through the samples. As shown in Figure 2.1-1, a 2020 argon-ion laser was used to excite the Eu^{3+} ions. The 457.9 nm line from the laser was used to excite the Eu^{3+} ions in these samples from the ${}^7\text{F}_0$ ground state to the ${}^5\text{D}_2$ excited state (Figure-3).

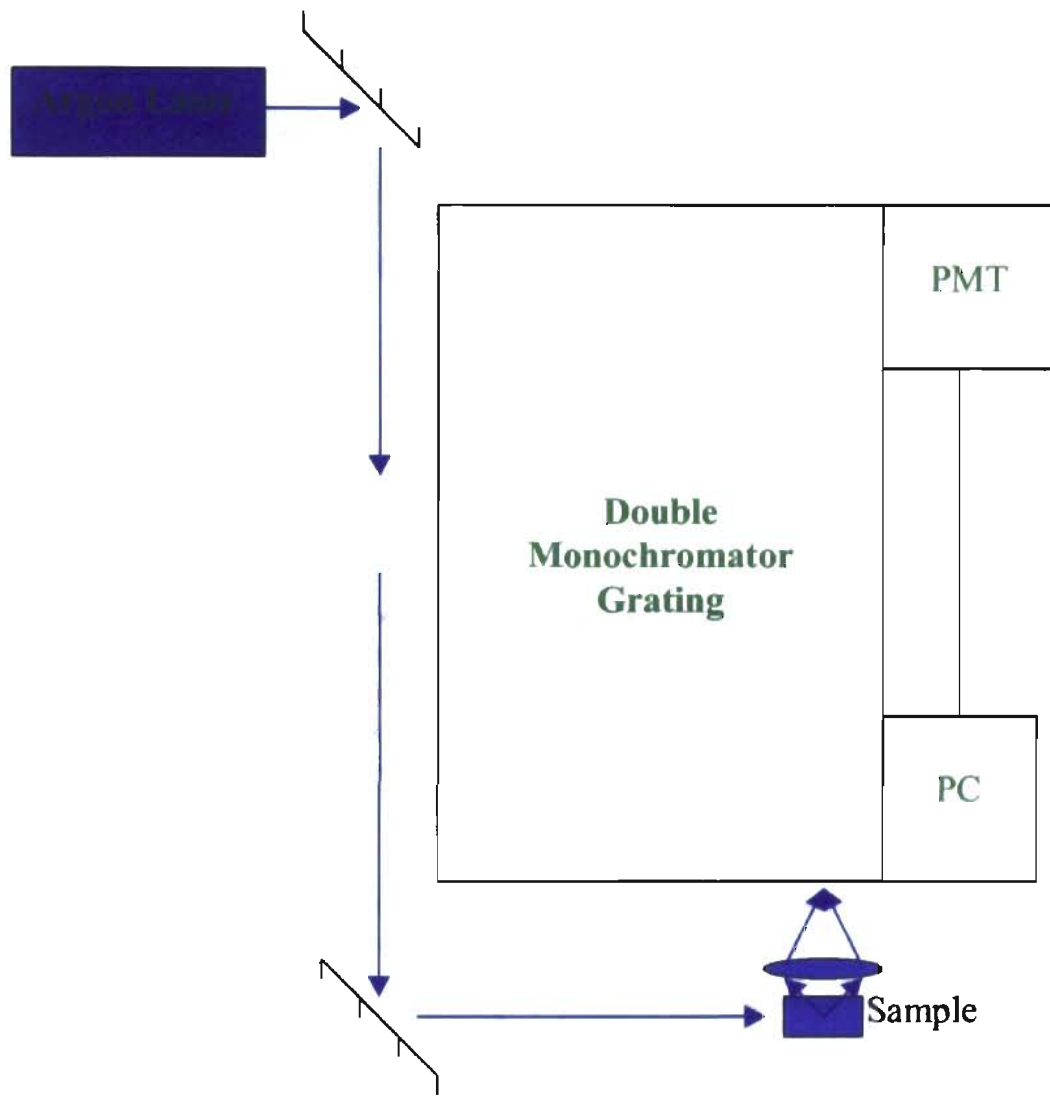


Figure-2: Experimental Setup for Fluorescence Transition measurements.

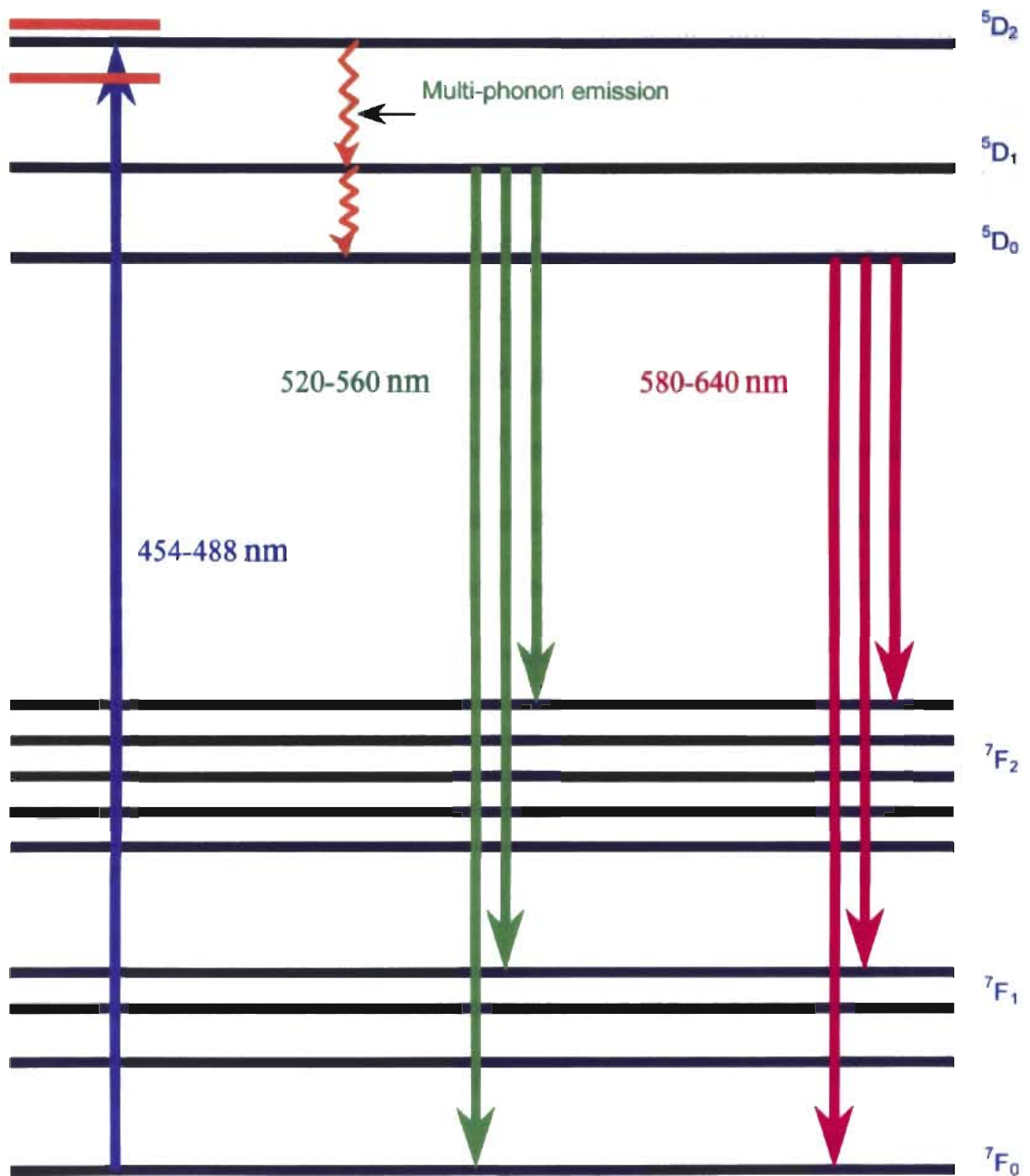


Figure-3: Eu^{3+} energy level diagram.

The fluorescent light was directed into a Jobin-Yvon Ramanor U-1000 spectrometer, which was connected to a photomultiplier tube and interfaced to a 486-computer for the data acquisition purpose. We first calibrated the spectrometer with a given reference at 514.5 nm. Experiments were conducted in two different ranges,

a) 2000 cm^{-1} to 4100 cm^{-1} (relative to the 457.9 nm laser line)

b) 4100 cm^{-1} to 7000 cm^{-1} (relative to the 457.9 nm laser line)

In the first range, the step size was 2 cm^{-1} , and the time interval between successive counts was 1 sec. In the second range, the step size was 4 cm^{-1} , and the time interval remained the same. The laser power used for both ranges was the same (60mW or 80mW). Each of the four spectrometer slits were set at 200 microns.

2.4 Absorption Measurements:

Absorption measurements were conducted on the samples described in section 2.1 at room temperature (20°C) and at -183°C . A Cary 5 spectrophotometer was used for the absorption measurements.

Samples were cleaned with acetone and placed on a holder which was then positioned in the spectrophotometer. Sample holders had an aperture of 1 mm in diameter. The spectrophotometer scanned the wavelength range from 250 nm to 650 nm in steps of 0.2 nm. The time interval between successive steps was 1 second. Prior to each scan, a base line correction had been conducted for the same wavelength range, step size and time interval as mentioned above. The Cary 5 Spectrophotometer was interfaced with a computer that used a Lotus style software for the purpose of data acquisition.

For the samples the absorption measurements were carried out at -183°C . Samples were first cleaned and placed into the sample holders of the cryostat. The samples were also

pressed between two metal disks, which had circular apertures (of diameter 1 mm) which exactly matched the sample holders used for the baseline correction. The height of the sample was then adjusted so that light could pass through the sample unobstructed.

RESULTS:

3.1 Density and Number Density:

In section 2.1 we discussed how the densities of each sample were calculated. In Table 3.1-a, 3.1-b, 3.1-c and 3.1-d we have tabulated those values, along with the number densities of each sample.

To calculate the number density of a sample, the following formulae was used

$$\text{NumberDensity} = \frac{\text{Density}}{\text{MolecularWeight}} \times 6.023 \times 10^{23} \times \left(2 \times \text{Eu}_2\text{O}_3 \text{ in mole\%} \times \frac{1}{100} \right)$$

Table 3.1-a: Density and Number Density (Eu³⁺ Series)

Eu ³⁺ Series (in mole%)	Density (gm/cm ³)	Number density (10 ²¹ /cm ³)
1.5%	2.566±0.004	0.728±0.064
2.5%	2.664±0.004	1.205±0.064
5.0%	2.778±0.004	2.264±0.064
7.5%	2.845±0.004	3.165±0.064
10.0%	3.000±0.004	4.082±0.064
15.0%	3.329±0.004	5.831±0.064

Table 3.1-b: Density and Number Density (Al Series)

Al Series (in mole%)	Density (gm/ cm ³)	Number density (10 ²¹ /cm ³)
0.000%	2.598±0.004	1.197±0.064
5.850%	2.627±0.004	1.167±0.064
8.775%	2.678±0.004	1.168±0.064
14.625%	2.781±0.004	1.171±0.064

Table 3.1-c: Density and Number Density (Na⁺ Series)

Na ⁺ Series (in mole%)	Density (gm/ cm ³)	Number density (10 ²¹ /cm ³)
9.750	2.574±0.004	1.166±0.064
19.500	2.605±0.004	1.176±0.064
24.375	2.682±0.004	1.210±0.064

Table 3.1-d: Density and Number Density (Sample: OPT)

Sample	Density (gm/ cm ³)	Number density (10 ²¹ /cm ³)
OPT	3.047±0.004	3.944±0.064

3.2 Fluorescence Results:

We have studied fluorescence at room temperature (20⁰C) and at -35⁰C for all the samples of the first two series mentioned in section 2.1. Only room temperature results were obtained for the third series. Fluorescent measurements at 20⁰C and at -183⁰C were performed on the OPT sample. We also have mentioned that the fluorescent measurements were done in two different ranges (2000 to 4100 cm⁻¹ and 4100 to 7000 cm⁻¹) relative to the 457.9 nm laser line. In the first range (2000 to 4100 cm⁻¹) fluorescence transitions (⁵D₁→⁷F_J) are due to radiative transitions originating from the ⁵D₁ multiplets. Background counts were subtracted from the normalized data (normalized with respect to the transition ⁵D₂→⁷F₃) and then plotted with the aid of Sigma Plot (Figure-4). During plotting a program was employed to convert wavenumbers to wavelengths.

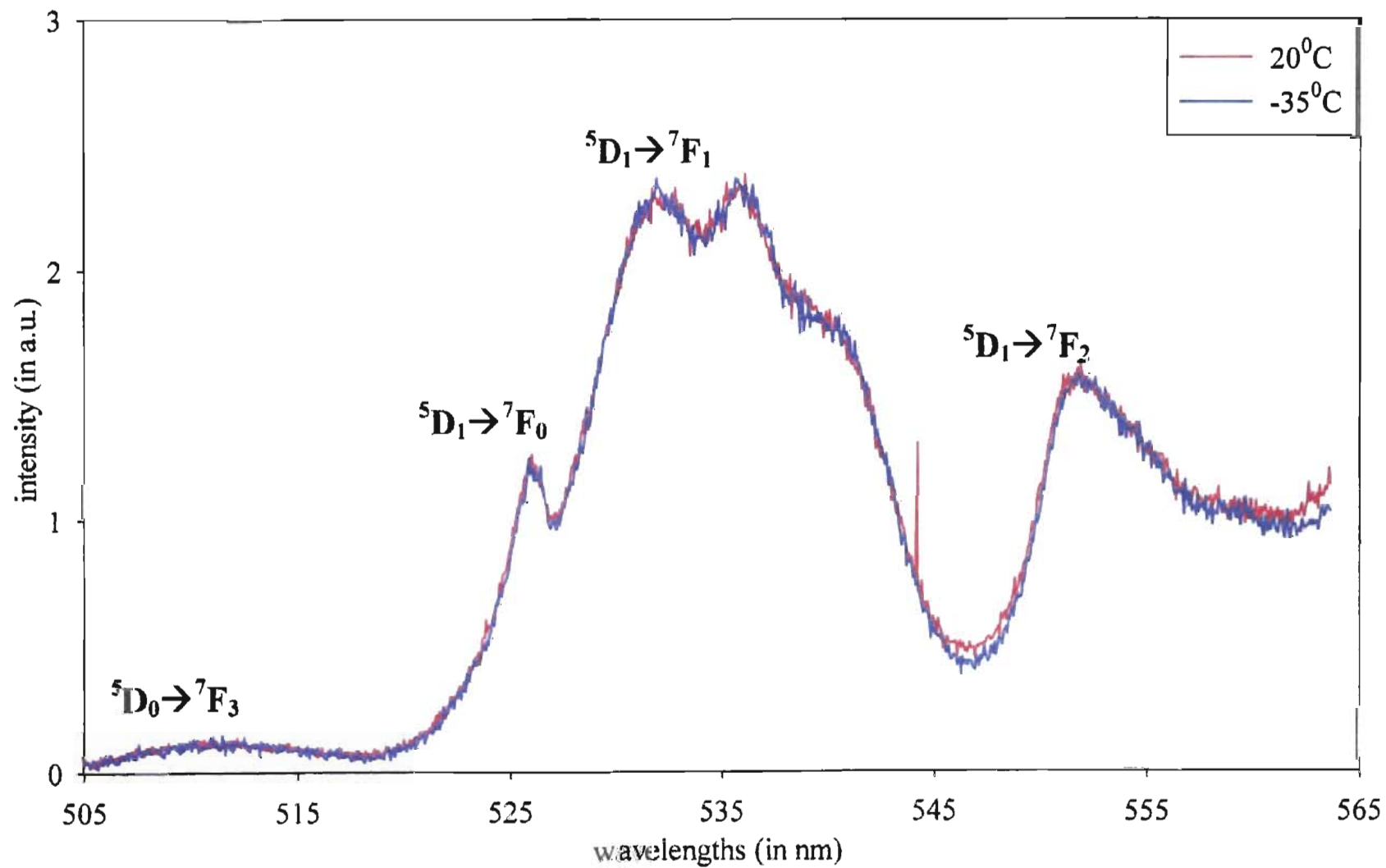


Figure-4: Fluorescence Transitions (Region I, Sample: 1.5 mole% of Eu^{3+})

The Microcal Origin software was used to determine the integrated intensity for the observed fluorescence transitions. Ratio calculations of the integrated intensity of the fluorescence transitions have been carried out within the same scan, so that any changes in the sample position or environmental effects have been minimized. In the first range (2000 to 4100 cm^{-1}), the following ratios have been computed:

a) ${}^5\text{D}_1 \rightarrow {}^7\text{F}_0$ to ${}^5\text{D}_1 \rightarrow {}^7\text{F}_1$ and

b) ${}^5\text{D}_1 \rightarrow {}^7\text{F}_2$ to ${}^5\text{D}_1 \rightarrow {}^7\text{F}_1$

These ratios have been calculated at room temperature for all the samples and at -35°C for the first two series. These ratio calculations are tabulated in the Table 3.2-a through Table 3.2-e.

Table 3.2-a: Integrated Intensity Ratio (Eu^{3+} Series): Region-I (20°C)

Eu^{3+} Series (in mole%)	${}^5\text{D}_1 \rightarrow {}^7\text{F}_0 / {}^5\text{D}_1 \rightarrow {}^7\text{F}_1$	${}^5\text{D}_1 \rightarrow {}^7\text{F}_2 / {}^5\text{D}_1 \rightarrow {}^7\text{F}_1$
1.5%	0.140	0.278
2.5%	0.119	0.316
5.0%	0.141	0.369
7.5%	0.124	0.358
10.0%	0.131	0.300
15.0%	0.156	0.358

Table 3.2-b: Integrated Intensity Ratio (Eu³⁺ Series): Region-I (-35⁰C)

Eu ³⁺ Series (in mole%)	${}^5D_1 \rightarrow {}^7F_0 / {}^5D_1 \rightarrow {}^7F_1$	${}^5D_1 \rightarrow {}^7F_2 / {}^5D_1 \rightarrow {}^7F_1$
1.5%	0.141	0.270
2.5%	0.121	0.306
5.0%	0.151	0.364
7.5%	0.138	0.388
10.0%	0.148	0.300
15.0%	0.180	0.351

Table 3.2-c: Integrated Intensity Ratio (Al Series): Region-I (20⁰C)

Al series (in mole%)	${}^5D_1 \rightarrow {}^7F_0 / {}^5D_1 \rightarrow {}^7F_1$	${}^5D_1 \rightarrow {}^7F_2 / {}^5D_1 \rightarrow {}^7F_1$
0.000	0.170	0.356
5.850	0.185	0.403
8.775	0.241	0.425
14.625	0.252	0.469

Table 3.2-d: Integrated Intensity Ratio (Al Series): Region-I (-35⁰C)

Al series (in mole%)	${}^5D_1 \rightarrow {}^7F_0 / {}^5D_1 \rightarrow {}^7F_1$	${}^5D_1 \rightarrow {}^7F_2 / {}^5D_1 \rightarrow {}^7F_1$
0.000	0.198	0.397
5.850	0.193	0.404
8.775	0.202	0.347
14.625	0.254	0.469

Table 3.2-e: Integrated Intensity Ratio (Na⁺ Series): Region-I (20^oC)

Na ⁺ series (in mole%)	${}^5D_1 \rightarrow {}^7F_0 / {}^5D_1 \rightarrow {}^7F_1$	${}^5D_1 \rightarrow {}^7F_2 / {}^5D_1 \rightarrow {}^7F_1$
9.750	0.194	0.390
19.500	0.130	0.352
24.375	0.122	0.312

In the second range (4100 to 7000 cm⁻¹) the fluorescence transitions originate from the 5D_0 excited state. In this range (Figure-5), the data were individually fed into Sigma Plot. Room temperature data and low temperature data were normalized with respect to the transition ${}^5D_2 \rightarrow {}^7F_3$ because temperature variation had a very little effect on this transition. We input the data into the peak fit program and determined the relative peak intensity ratios. Again we have done the ratio calculations within the same scan, so that any changes in the sample position or environmental effects have been minimized. In this range (4100 cm⁻¹ to 7000 cm⁻¹) we have computed the following ratios:

- a) ${}^5D_0 \rightarrow {}^7F_2$ to ${}^5D_0 \rightarrow {}^7F_1$
- b) ${}^5D_0 \rightarrow {}^7F_0$ to ${}^5D_0 \rightarrow {}^7F_1$ and
- c) ${}^5D_0 \rightarrow {}^7F_3$ to ${}^5D_0 \rightarrow {}^7F_1$

As mentioned, we have calculated these ratios both at room temperature and at -35^oC for all the series except the Na⁺ series for which only the room temperature were available. The integrated intensity ratio values for the transitions ${}^5D_0 \rightarrow {}^7F_0 / {}^5D_0 \rightarrow {}^7F_1$ and ${}^5D_0 \rightarrow {}^7F_3 / {}^5D_0 \rightarrow {}^7F_1$ for the varying Eu³⁺, Al and Na⁺ series are tabulated in the Tables 3.2-f through Table 3.2-j. The ratio values for the transitions ${}^5D_0 \rightarrow {}^7F_2 / {}^5D_0 \rightarrow {}^7F_1$ are tabulated in Tables 3.2-k through Table 3.2-0.

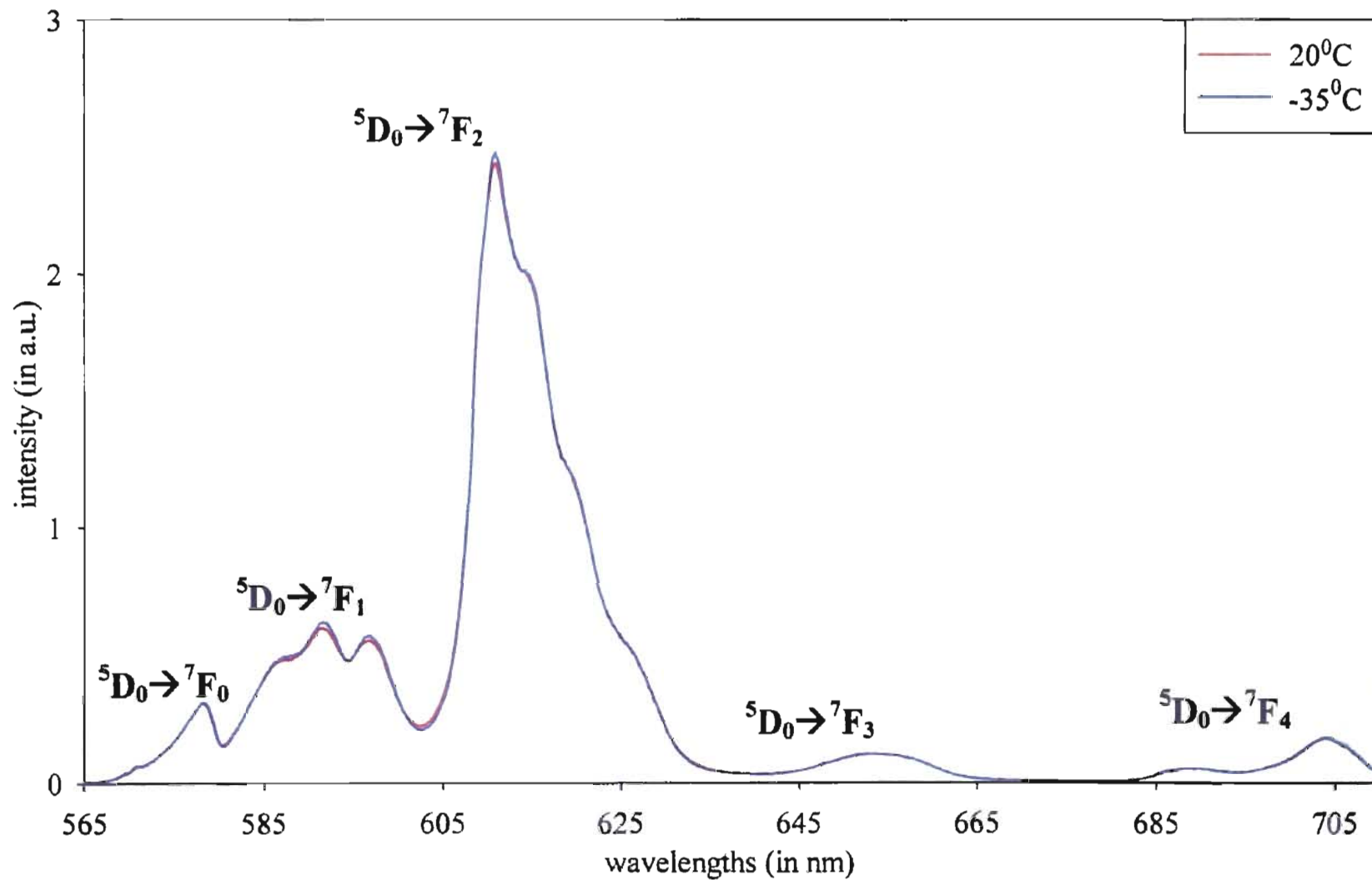


Figure-5: Fluorescence Transitions (Region II, Sample: 1.5 mole% of Eu^{3+})

Table 3.2-f: Integrated Intensity Ratio (Eu³⁺ Series): Region-II (20⁰C)

Eu ³⁺ Series (in mole%)	${}^5D_0 \rightarrow {}^7F_0 / {}^5D_0 \rightarrow {}^7F_1$	${}^5D_0 \rightarrow {}^7F_3 / {}^5D_0 \rightarrow {}^7F_1$
1.5%	0.179	0.176
2.5%	0.140	0.200
5.0%	0.141	0.176
7.5%	0.146	0.182
10.0%	0.127	0.171
15.0%	0.146	0.187

Table 3.2-g: Integrated Intensity Ratio (Eu³⁺ Series): Region-II (-35⁰C)

Eu ³⁺ Series (in mole%)	${}^5D_0 \rightarrow {}^7F_0 / {}^5D_0 \rightarrow {}^7F_1$	${}^5D_0 \rightarrow {}^7F_3 / {}^5D_0 \rightarrow {}^7F_1$
1.5%	0.176	0.172
2.5%	0.137	0.189
5.0%	0.139	0.177
7.5%	0.144	0.169
10.0%	0.121	0.164
15.0%	0.140	0.185

Table 3.2-h: Integrated Intensity Ratio (Al Series): Region-II (20⁰C)

Al series (in mole%)	${}^5D_0 \rightarrow {}^7F_0 / {}^5D_0 \rightarrow {}^7F_1$	${}^5D_0 \rightarrow {}^7F_3 / {}^5D_0 \rightarrow {}^7F_1$
0.000	0.140	0.172
5.850	0.171	0.192
8.775	0.190	0.162
14.625	0.239	0.180

Table 3.2-i: Integrated Intensity Ratio (Al Series): Region-II (-35⁰C)

Al series (in mole%)	${}^5D_0 \rightarrow {}^7F_0 / {}^5D_0 \rightarrow {}^7F_1$	${}^5D_0 \rightarrow {}^7F_3 / {}^5D_0 \rightarrow {}^7F_1$
0.000	0.138	0.170
5.850	0.168	0.190
8.775	0.187	0.164
14.625	0.225	0.171

Table 3.2-j: Integrated Intensity Ratio (Na⁺ Series): Region-II (20⁰C)

Na ⁺ series (mole%)	${}^5D_0 \rightarrow {}^7F_0 / {}^5D_0 \rightarrow {}^7F_1$	${}^5D_0 \rightarrow {}^7F_3 / {}^5D_0 \rightarrow {}^7F_1$
9.750	0.199	0.198
19.500	0.129	0.165
24.375	0.116	0.163

Table 3.2-k: Integrated Intensity Ratio (Eu³⁺ Series): Region-II (20⁰C)

Eu ³⁺ Series (mole%)	${}^5D_0 \rightarrow {}^7F_2 / {}^5D_0 \rightarrow {}^7F_1$
1.5	3.308
2.5	3.483
5.0	3.490
7.5	3.485
10.0	3.504
15.0	3.587

Table 3.2-l: Integrated Intensity Ratio (Eu³⁺ Series): Region-II (-35⁰C)

Eu ³⁺ Series (mole%)	${}^5D_0 \rightarrow {}^7F_2 / {}^5D_0 \rightarrow {}^7F_1$
1.5	3.255
2.5	3.419
5.0	3.462
7.5	3.448
10.0	3.450
15.0	3.598

Table 3.2-m: Integrated Intensity Ratio (Al Series): Region-II (20⁰C)

Al series (in mole%)	${}^5D_0 \rightarrow {}^7F_2 / {}^5D_0 \rightarrow {}^7F_1$	${}^5D_2 \rightarrow {}^7F_3 / {}^5D_0 \rightarrow {}^7F_1$
0.000	3.313	-
5.850	3.513	-
8.775	3.600	0.020
14.625	3.438	0.051

Table 3.2-n: Integrated Intensity Ratio (Al Series): Region-II (-35⁰C)

Al series (in mole%)	${}^5D_0 \rightarrow {}^7F_2 / {}^5D_0 \rightarrow {}^7F_1$	${}^5D_2 \rightarrow {}^7F_3 / {}^5D_0 \rightarrow {}^7F_1$
0.000	3.270	-
5.850	3.477	0.015
8.775	3.583	0.022
14.625	3.412	0.055

Table 3.2-o: Integrated Intensity Ratio (Na⁺ Series): Region-II (20.0^oC)

Na ⁺ Series (in mole%)	${}^5D_0 \rightarrow {}^7F_2 / {}^5D_0 \rightarrow {}^7F_1$
9.750	3.629
19.500	3.229
24.375	3.277

For the special sample OPT , room temperature (upper row in the Table 3.2-p) and liquid nitrogen temperature (lower row in the Table 3.2-p) ratio calculations have been carried out. A sharp transition (${}^5D_2 \rightarrow {}^7F_5$) at liquid nitrogen temperature for the sample OPT (Figure-6) has been observed at around 570 nm .

Table 3.2-p: Integrated Intensity Ratio (sample: OPT)

${}^5D_2 \rightarrow {}^7F_5 / {}^5D_0 \rightarrow {}^7F_1$	${}^5D_0 \rightarrow {}^7F_0 / {}^5D_0 \rightarrow {}^7F_1$	${}^5D_0 \rightarrow {}^7F_2 / {}^5D_0 \rightarrow {}^7F_1$	${}^5D_0 \rightarrow {}^7F_3 / {}^5D_0 \rightarrow {}^7F_1$
0.092 (20 ^o C)	0.325	3.460	0.198
0.102 (-183 ^o C)	0.260	3.321	0.185

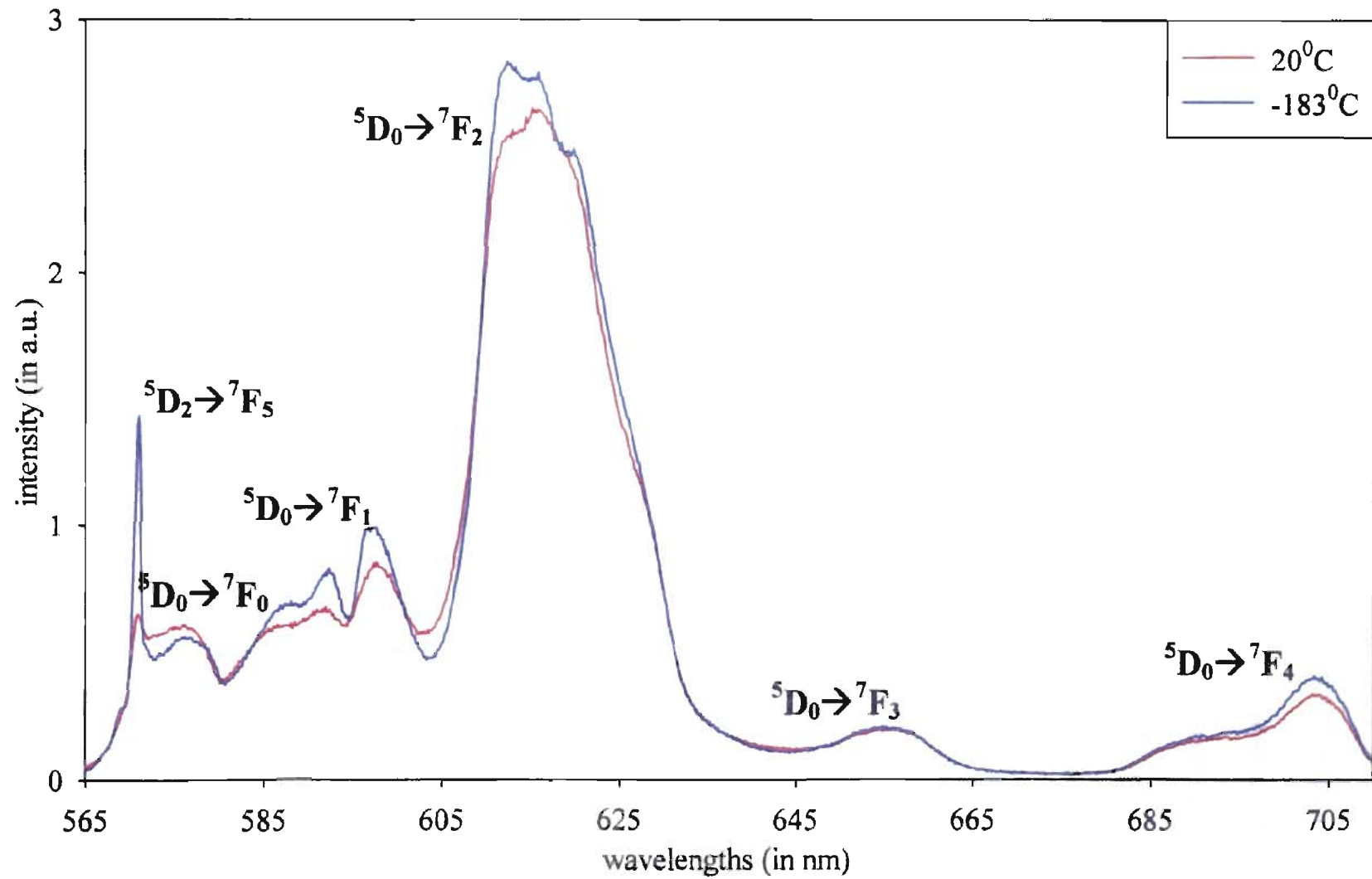


Figure-6: Fluorescence Transitions (Region II, Sample: OPT)

3.3 Absorption Results:

Absorption measurements have been carried out with a Cary-5 spectrophotometer, and the data acquisition part has been conducted using a computer interfaced to the system. The data gives us the total absorption through the sample as a function of wavelength. To obtain the absorption coefficient, we divided the absorption data by the respective glass sample thickness. As mentioned the data ranges from 250 nm to 650 nm (Figure-7). The absorption transition lines, ${}^7F_0 \rightarrow {}^5D_2$, ${}^7F_0 \rightarrow {}^5D_4$ and ${}^7F_0 \rightarrow {}^5L_6$ were used to obtain the integrated absorbance of an electric dipole. The data were divided into three smaller regions around each of these transition lines. Using Sigma Plot software and Peak Fit software, the area beneath each of these absorption transitions (Figure-8 through Figure-10) were calculated. The area beneath each of these absorption transition lines represent the integrated absorbance of an electric dipole and were calculated as follows (Figure-11):

- a) Input the absorption curve into peak fit in order to compute the area under the curve.
- b) Next, all data points around the transition lines have been removed and then the remaining data points were fitted with Sigma Plot using an inverse third order polynomial. The area under the smoothed curved was again determined by the Peak Fit software.
- c) Take the difference of the results of a) and b) to determine the area beneath the transition lines.

The following two equations^[9] have been employed to compute the Judd-Offelt^[6,7] parameters.

$$\int k(\lambda) d\lambda = N \frac{8\pi^3 e^2 \bar{\lambda}}{3ch(2J+1)} \frac{(n^2 + 2)^2}{9n} S \quad (3.3.1)$$

Here the $\int k(\lambda)$ is the integrated absorbance of an electric dipole, $\bar{\lambda}$ is the mean wave length of each respective transitions, n is the refractive index of the material for that particular wavelength and S is the oscillator strength.

$$S = \sum_{t=2,4,6} \Omega_t \left| \langle (S, L) J \| U^{(t)} \| (S', L') J' \rangle \right|^2, \quad (3.3.2)$$

where the elements $\langle \| U^{(t)} \| \rangle$ are the doubly reduced unit tensor operators calculated^[9] in the intermediate-coupling approximation. The refractive index used for all the samples used was 1.55 because for similar samples, values around 1.55 had been observed in our laboratory and the variations were negligible. Mean wavelength of each transition lines were computed from the peak fitted graphs.

Along with the calculated values of the integrated absorbance of the electric dipoles and refractive index of the samples, the values of the doubly reduced unit tensor operators calculated in the intermediate-coupling approximation were taken from Carnall et. al..^[10]

The calculated values of the Judd-Offelt^[6,7] parameters at room temperature are tabulated in Tables 3.3-a, 3.3-b, 3.3-c and 3.3-d.

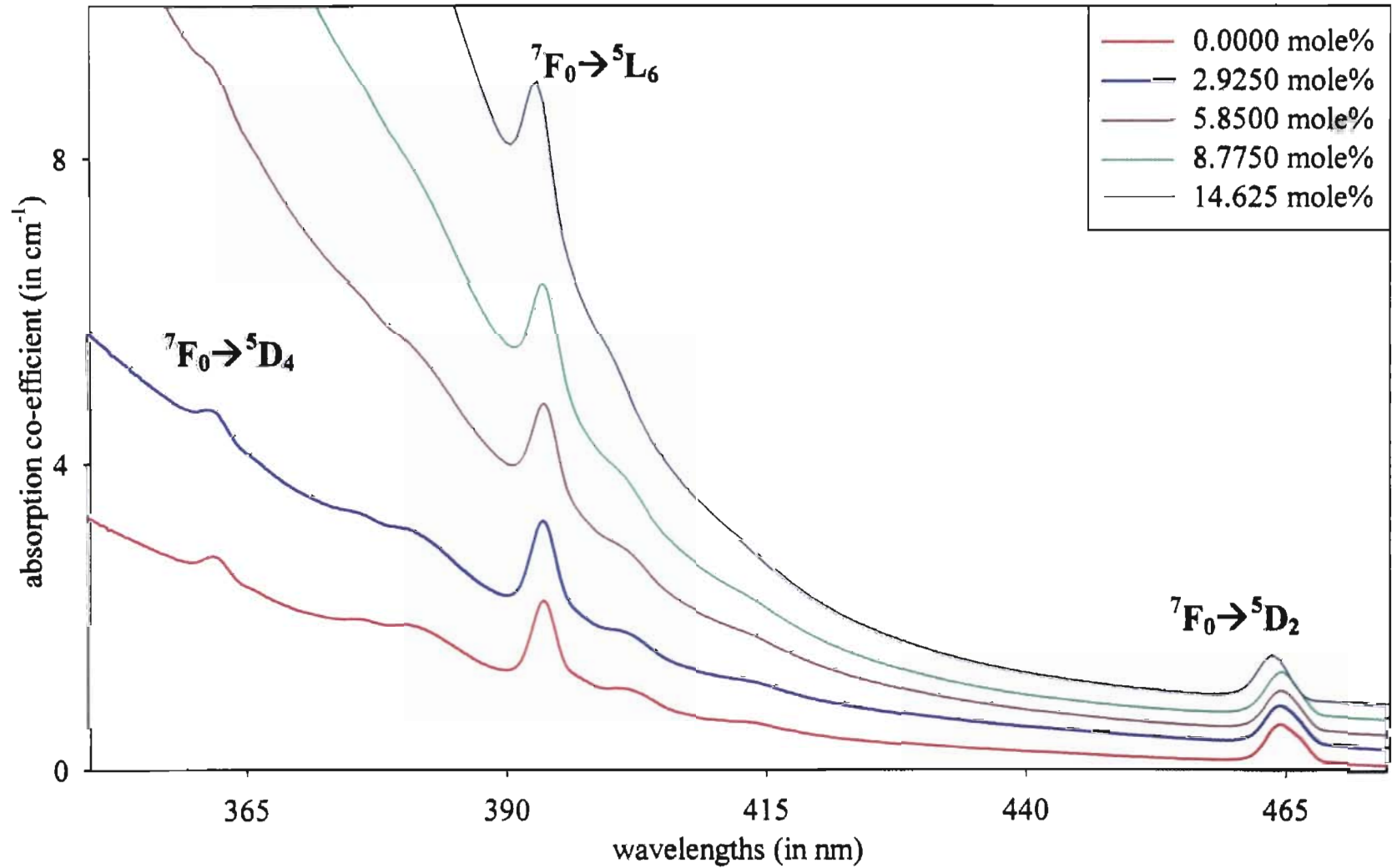


Figure-7: Absorption Transitions (Al Series)

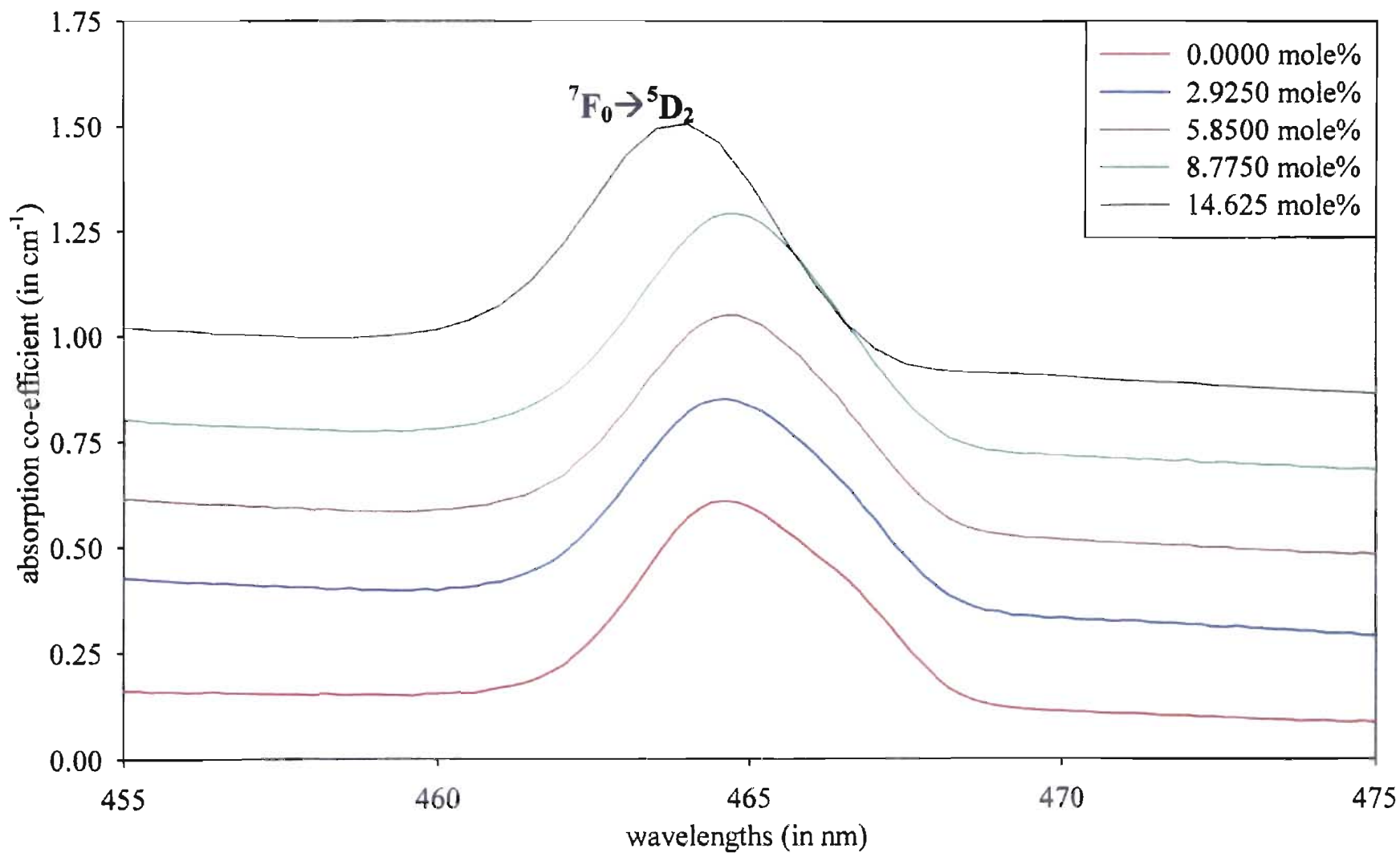


Figure-8: ${}^7F_0 \rightarrow {}^5D_2$ Absorption Transitions (Al Series)

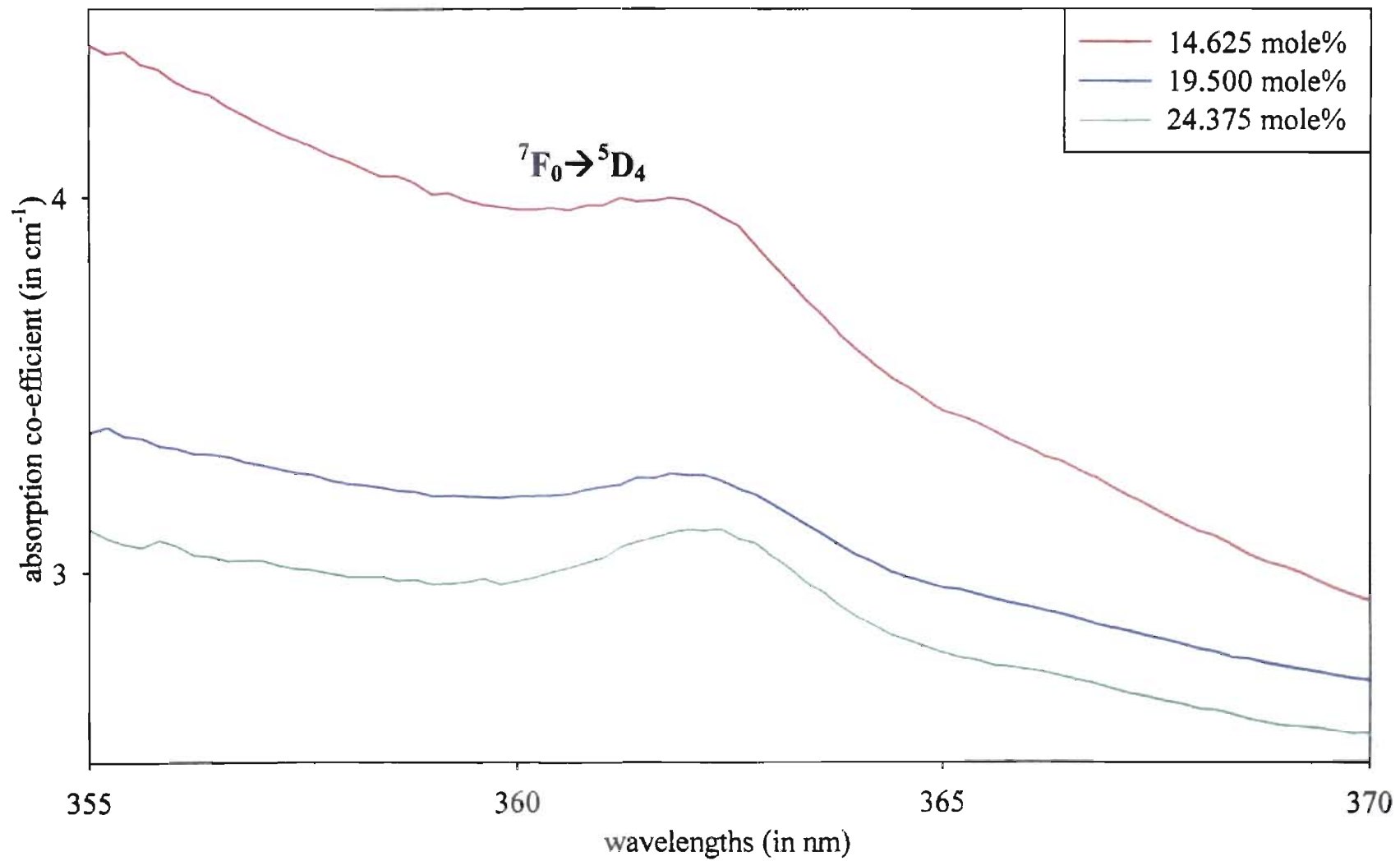


Figure-9: ${}^7F_0 \rightarrow {}^5D_4$ Absorption Transitions (Na^+ Series)

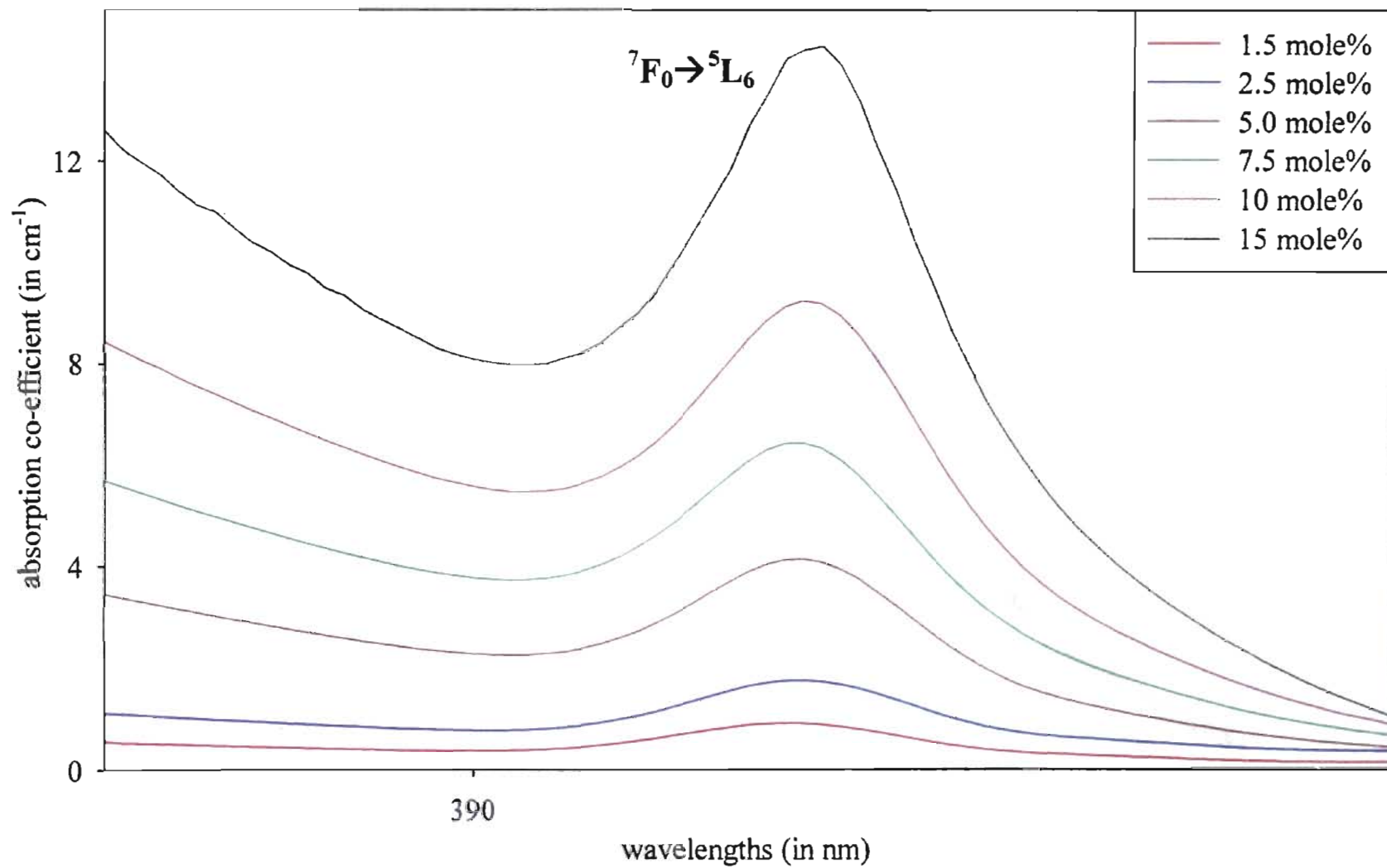


Figure-10: ${}^7F_0 \rightarrow {}^5L_6$ Absorption Transitions (Eu^{3+} Series)

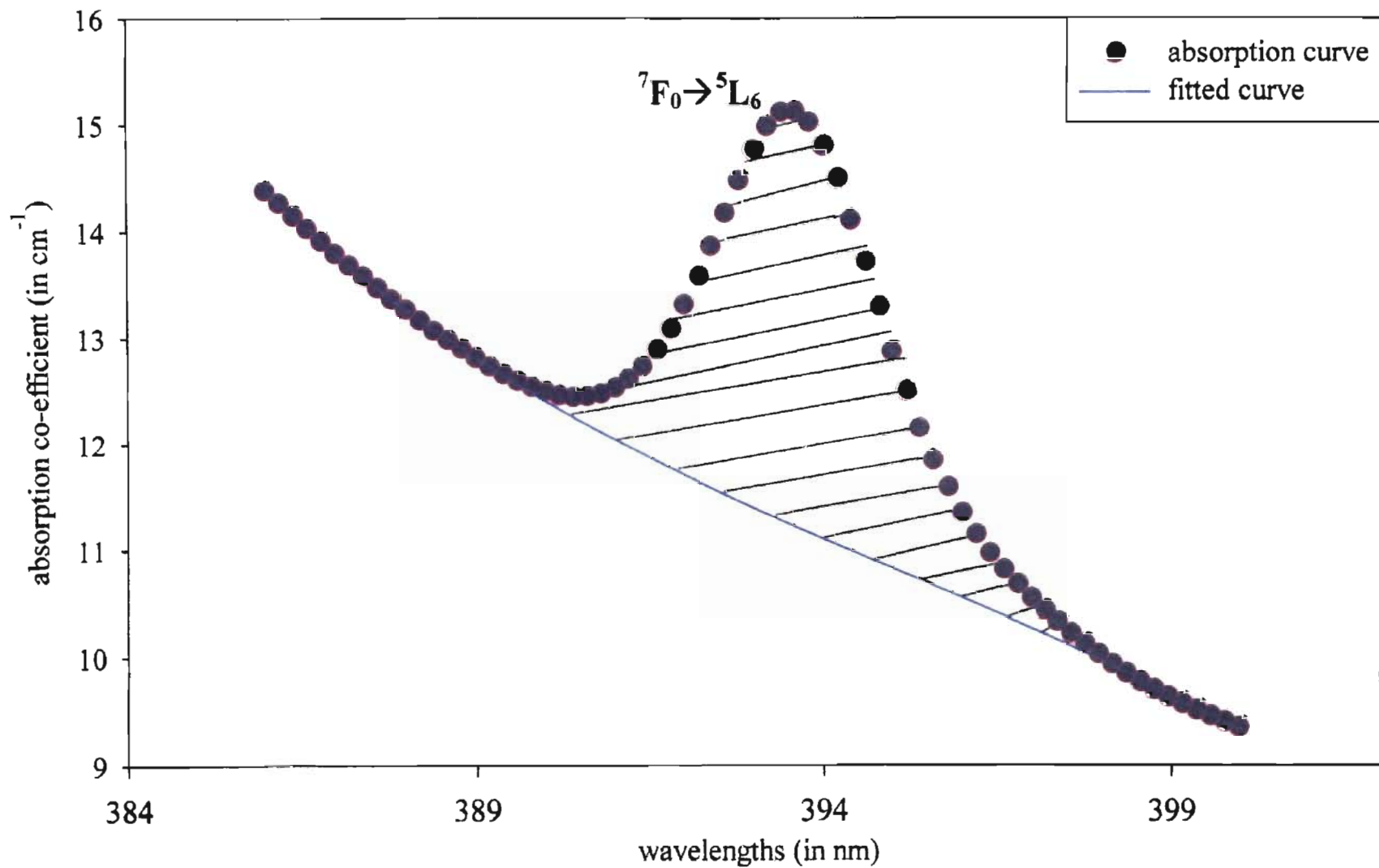


Figure-11: ${}^7F_0 \rightarrow {}^5L_6$ Absorption X-section (7.5 mole% of Eu^{3+})

Table 3.3-a: Judd-Offelt Parameters (Eu³⁺ Series)

Eu ³⁺ series in mole%	Refractive index	Ω_2 (in 10 ⁻²⁰) in cm ²	Ω_4 (in 10 ⁻²⁰) in cm ²	Ω_6 (in 10 ⁻²⁰) in cm ²
1.5%	1.55±0.1	5.1±0.4	1.24±0.15	0.501±0.038
2.5%	1.55±0.1	4.8±0.4	-	0.524±0.038
5.0%	1.55±0.1	5.3±0.4	1.53±0.15	0.625±0.038
7.5%	1.55±0.1	5.3±0.4	-	0.669±0.038
10.0%	1.55±0.1	6.1±0.4	-	0.722±0.038
15.0%	1.55±0.1	6.2±0.4	-	0.792±0.038

Table 3.3-b: Judd-Offelt Parameters (Al Series)

Al series (in mole%)	Refractive index	Ω_2 (in 10 ⁻²⁰) in cm ²	Ω_4 (in 10 ⁻²⁰) in cm ²	Ω_6 (in 10 ⁻²⁰) in cm ²
0.000	1.55	4.5±0.4	1.95±0.25	0.460±0.038
5.850	1.55	4.9±0.4	2.30±0.25	0.570±0.038
8.775	1.55	5.3±0.4	3.13±0.30	0.649±0.038
14.625	1.55	5.1±0.4	-	0.824±0.038

Table 3.3-c: Judd-Offelt Parameters (Na⁺ Series)

Na ⁺ series (in mole%)	Refractive index	Ω_2 (in 10 ⁻²⁰) in cm ²	Ω_4 (in 10 ⁻²⁰) in cm ²	Ω_6 (in 10 ⁻²⁰) in cm ²
9.750	1.55	4.1±0.4	-	0.392±0.038
19.500	1.55	3.7±0.4	1.11±0.15	0.395±0.038
24.375	1.55	4.6±0.4	1.54±0.15	0.428±0.038

Judd-Offelt^[6,7] parameters were also calculated and are tabulated (Table 3.3-e) for the special sample OPT at room temperature (upper row) and at liquid nitrogen temperature (bottom row).

Table 3.3-d: Judd-Offelt Parameters (Sample: OPT)

Ω_2 (in 10^{-20}) in cm^2	Ω_4 (in 10^{-20}) in cm^2	Ω_6 (in 10^{-20}) in cm^2
3.3 ± 0.4 (20°C)	-	0.605 ± 0.038
5.0 ± 0.4 (-183°C)	-	0.857 ± 0.038

DISCUSSION:

Number density is directly proportional to density and inversely proportional to the sum of the molecular weights of the constituents of the glass samples used in the experiments. So any increase in density results in an increase in the number density, whereas any increase in the sum of the molecular weights of the constituent atoms of the glass sample results in a decrease in the number density. Since an increase or decrease in the concentrations of Eu^{3+} , Al and Na^+ was compensated by a decrease or increase in the concentration of silica, the molecular weight of the samples can be varied more effectively by varying the Eu^{3+} concentration rather than introducing a variation either by Al or Na^+ . Also from, section 3.1, for glass samples number density is seen to be directly proportional to the Eu^{3+} concentration.

Density measurements were accomplished using Archimedes' Principle. Water at room temperature was used to measure the volume of the samples with a base density for calculation of $1\text{gm}/\text{cm}^3$. Calculated results of the density measurements are presented in Tables 3.1-a through Table 3.1-d. It was observed that with increasing Eu^{3+} ion concentration, both density and molecular weight increased with the net effect that the number density increased nearly linearly.

For the Al varying series, density changes were insignificant since the change in mole percentage of aluminum was done at the expense of silica and both have nearly the same molecular weight. The number density did not vary considerably as the concentration of the Eu^{3+} remained the same through out the series. The same trend was observed for the Na^+ ion varying series.

The density and number density of the sample OPT are tabulated in Table 3-d.

Fluorescence:

Ground level electrons were populated to excited states and then fluorescence was observed. The 457.9 nm laser line was used to excite the ground level 7F_0 (and possibly the 7F_1 and 7F_2) electrons to 5D_2 (slightly higher) state. Electrons from 5D_2 state decay non-radiatively to 5D_1 state and similarly to 5D_0 state by multi-phonon emission^[11] from which radiative decay to 7F_J multiplets took place. Observed radiative transitions from 5D_1 to 7F_J multiplets are shown in Figure 3.2-1. Ratio calculation of ${}^5D_1 \rightarrow {}^7F_0 / {}^5D_1 \rightarrow {}^7F_1$ and ${}^5D_1 \rightarrow {}^7F_2 / {}^5D_1 \rightarrow {}^7F_1$ are tabulated in Table-3.2-a through Table 3.2-e.

As mentioned above due to non-radiative decay from ${}^5D_2 \rightarrow {}^5D_1$ and then from ${}^5D_1 \rightarrow {}^5D_0$ state, ${}^5D_1 \rightarrow {}^7F_J$ radiative transitions are very weak. For the Eu^{3+} series the integrated intensity ratio of ${}^5D_1 \rightarrow {}^7F_0 / {}^5D_1 \rightarrow {}^7F_1$ transitions shows that low temperature transition ratio values are more than those of the room temperature ratio values. It is also observed that for each sample of the Eu^{3+} series ${}^5D_1 \rightarrow {}^7F_0 / {}^5D_1 \rightarrow {}^7F_2$, values increase with decreasing the temperature (results of these calculations are not shown in Table format to avoid redundancy and can easily be calculated by dividing column II by column III of the tables). The integrated intensity ratio of the forced electric dipole transitions ${}^5D_1 \rightarrow {}^7F_2 / {}^5D_1 \rightarrow {}^7F_1$ did not show any particular trend and the percent difference among the ratio values at room temperature and at -35°C varied at most by 8% (for the 7.5mole% of Eu^{3+}). The ${}^5D_1 \rightarrow {}^7F_0$ transition is a magnetic dipole allowed transition and found to be more effective at low temperature than the forced electric dipole transitions ${}^5D_1 \rightarrow {}^7F_1$ and ${}^5D_1 \rightarrow {}^7F_2$. In the Al varying series it also was found that the same trend was followed and ${}^5D_1 \rightarrow {}^7F_0 / {}^5D_1 \rightarrow {}^7F_1$ values increased at

lower temperature for individual samples, while the integrated intensity ratio of the forced dipole transitions (${}^5D_1 \rightarrow {}^7F_1 / {}^5D_1 \rightarrow {}^7F_2$) remained almost the same. It was also observed from the Table 3.2-c and Table 3.2-d that the integrated intensity ratio values of the transitions ${}^5D_1 \rightarrow {}^7F_0 / {}^5D_1 \rightarrow {}^7F_1$ and ${}^5D_1 \rightarrow {}^7F_2 / {}^5D_1 \rightarrow {}^7F_1$ at both room and low temperature had the lowest values for minimum Al concentration and vice versa. It indicates that incorporating more Al has noticeable effect in particular on the ${}^5D_1 \rightarrow {}^7F_1$ radiative transition. Two reasons could be accounted for this, one is that the availability of high energy phonons decreases with increasing Al concentration^[12] thus increasing more radiative decay from the 5D_1 state and at the same time admixing of states may decrease because Aluminum incorporation decreases the disorder around Eu^{3+} ions in the glass^[13].

Table 3.3-e showed that at room temperature, increasing Na^+ ion concentration causes a decrease in the integrated intensity ratio values (${}^5D_1 \rightarrow {}^7F_0 / {}^5D_1 \rightarrow {}^7F_1$ and ${}^5D_1 \rightarrow {}^7F_2 / {}^5D_1 \rightarrow {}^7F_1$). Low temperature measurements were not carried out on these samples (Na^+ series).

For the wavelength range 565nm to 700nm, for all the samples, the following ratios have been calculated:

- a) ${}^5D_0 \rightarrow {}^7F_0 / {}^5D_0 \rightarrow {}^7F_1$
- b) ${}^5D_0 \rightarrow {}^7F_3 / {}^5D_0 \rightarrow {}^7F_1$
- c) ${}^5D_0 \rightarrow {}^7F_2 / {}^5D_0 \rightarrow {}^7F_1$

The ${}^5D_0 \rightarrow {}^7F_1$ transition is a magnetic dipole allowed transition and the ${}^5D_0 \rightarrow {}^7F_2$ transition is a forced electric dipole allowed transition. The latter one is a hypersensitive transition^[9,14] that is very sensitive to the change in the glass structure

around Eu^{3+} ion; therefore, the integrated intensity ratio of the transitions ${}^5\text{D}_0 \rightarrow {}^7\text{F}_2 / {}^5\text{D}_0 \rightarrow {}^7\text{F}_1$ is a measure of the local structure around Eu^{3+} ion in the glass samples^[9,14,15]. The ${}^5\text{D}_0 \rightarrow {}^7\text{F}_3$ transition was the least sensitive to temperature and was used for normalization while mapping room temperature and low temperature (-35°C) on the same graph (Figure-5). Another strange transition was observed (Figure-6) for the higher Al concentration and in particular for the OPT sample at a very low temperature (-183°C), which will be discussed at the latter part of this section.

The ${}^5\text{D}_0 \rightarrow {}^7\text{F}_0$ transition was at 578 nm. Since it is a transition between non-degenerate states no stark splitting was observed. In the ${}^5\text{D}_0 \rightarrow {}^7\text{F}_1$ and ${}^5\text{D}_0 \rightarrow {}^7\text{F}_2$ transitions at around 592 nm and 612 nm respectively, 3 and 5 stark splitting were found as expected. The stark splitting was especially well resolved at low temperature. Because of homogeneous and inhomogeneous broadening, ${}^5\text{D}_0 \rightarrow {}^7\text{F}_1$ and ${}^5\text{D}_0 \rightarrow {}^7\text{F}_2$ transitions were found to be broad.

Like region-I, in the region-II, the integrated intensity ratios (Tables 3.2-f through Table-i) for the transitions ${}^5\text{D}_0 \rightarrow {}^7\text{F}_0 / {}^5\text{D}_0 \rightarrow {}^7\text{F}_1$ and ${}^5\text{D}_0 \rightarrow {}^7\text{F}_3 / {}^5\text{D}_0 \rightarrow {}^7\text{F}_1$ showed the similar trend that the room temperature values are lower than those of low temperature values. The forced electric dipole transitions are entirely dependent on mixing of states, i.e. mixing of $4f^N$ configurations with $4f^{N-1}5d$ or $4f^{N-1}5g$ states. This mixing so far may be accomplished by the static crystal field potential or by the vibrational interaction^[7]. The lower ratio values at lower temperature may result from a decrease in the vibrational interaction contribution.

The ratio values of the transitions ${}^5\text{D}_0 \rightarrow {}^7\text{F}_0 / {}^5\text{D}_0 \rightarrow {}^7\text{F}_1$ (Table 3.2-j) increases with increasing Al concentration . Incorporating Al_2O_3 results in structural evolution of the

sample^[12], which may account for this behavior. The incorporation of modifiers Eu^{3+} and Na^+ showed opposite trends though did not adhere strictly. The addition of Eu^{3+} and Na^+ increases the number of NBO's^[16] and may result in increase in the non radiative decay from the higher states ($^5\text{D}_2$ and $^5\text{D}_1$) and will increase the population of the $^5\text{D}_0$ state^[11]. The $^5\text{D}_0 \rightarrow ^7\text{F}_0$ transition is not a parity allowed transition and Judd-Offelt's^[6,7] closure relations do not hold for this transition as well. It has been suggested that the transition be allowed by J-mixing^[14,17-19] and can borrow intensity^[20,21] from $^5\text{D}_0 \rightarrow ^7\text{F}_2$ and $^5\text{D}_0 \rightarrow ^7\text{F}_4$ transitions. The behavior of the calculated integrated intensity ratio of the transitions $^5\text{D}_0 \rightarrow ^7\text{F}_0 / ^5\text{D}_0 \rightarrow ^7\text{F}_1$ can not be completely understood unless the integrated intensity of the $^5\text{D}_0 \rightarrow ^7\text{F}_4$ transition (which has not been considered in this research work) is included. For the integrated intensity ratios for the transitions $^5\text{D}_0 \rightarrow ^7\text{F}_2 / ^5\text{D}_0 \rightarrow ^7\text{F}_1$ the higher the Eu^{3+} concentration, the higher the ratio values except for the 10 mole% of Eu^{3+} at room temperature and for the 5 mole% of Eu^{3+} at low temperature. In general, the values showed a clear increase of ratio values with increasing Eu^{3+} concentration. This behavior is in agreement with the previous paragraph's statement and affirms that disorder is enhanced with increasing modifier concentration. The increasing ratio values display increasing hypersensitivity^[9,15], which is in accordance with the absorption measurements (Table 3.3-a). The absorption measurements showed that the Ω_2 parameters increase with increasing Eu^{3+} concentration, which is an indication of increasing hypersensitivity^[9,14]. It was in general observed that the low temperature values of the ratios were lower than those of room temperature values, again implying that the mixing of states are weakened at low temperature. In the Al varying series the ratios

of the integrated intensity of the transitions ${}^5D_0 \rightarrow {}^7F_2$ / ${}^5D_0 \rightarrow {}^7F_1$ also supports the above statement (Table 3.3-m and Table 3.3-n). With increasing Al concentration, at room temperature, the ratio values increase (except at 14.625 mole% of Al). The same trend was observed at low temperature. Though not clear, the structural re-organization may be playing a role here.

In addition to all known transitions, almost all samples exhibit a transition at around 570 nm, which has not been reported early by any other researcher, and is found to be very sensitive to temperature changes. This radiative transition does not match with any transition from 5D_1 or 5D_0 state to 7F_J multiplets. The only possible transition is from 5D_2 to 7F_5 state. Since the transition observed has an energy that matches with the ${}^5D_2 \rightarrow {}^7F_5$ transition, we have tentatively designated it as the ${}^5D_2 \rightarrow {}^7F_5$ transition. It has been found that this transition is very much temperature sensitive (Figure-6). For the sample OPT, the ${}^5D_2 \rightarrow {}^7F_5$ transition has a line width of 50 cm^{-1} at low temperature (-183°C) whereas at room temperature the linewidth increases to as much as 100 cm^{-1} . This remarkably sharp transition at lower temperature was noticed for 14.625 mole% of Al concentration, in addition this peak was totally absent for 0.0 mole% of Al containing sample and also did not appear for higher (19.500 and 24.375 mole%) Na^+ containing sample. As observed, the ${}^5D_2 \rightarrow {}^7F_5$ transition peak intensity is almost 50% of the hypersensitive ${}^5D_2 \rightarrow {}^7F_0$ transition at liquid nitrogen temperature with a linewidth of 50 cm^{-1} .

The ${}^5D_2 \rightarrow {}^7F_5$ transition is unlikely to be observed unless the availability of high energy phonon decreases. The non-radiative transitions are influenced by the availability of phonons and the energy of the phonons. It is well known that

increasing Na^+ concentration results in increasing NBO^[16] (non bridging oxygen), thus enhancing more phonon assisted non radiative transitions. Increasing Al_2O_3 decrease the NBO's and forms Al-O-Si bond which is associated with decreased phonon energy^[12,13] thus decreasing the multi-phonon decay rate^[11]. These factors are in good agreement with the observed ${}^5\text{D}_2 \rightarrow {}^7\text{F}_5$ transition. At lower temperature, availability of high energy phonon decreases and consequently non-radiative transitions decreases. Henceforth, this transition is possibly from the ${}^5\text{D}_2$ multiplets, in harmony with the energy gap between the ${}^5\text{D}_2$ and the ${}^7\text{F}_5$ energy bands.

The other ratio values for the OPT sample followed the same trend, that is at lower temperature the integrated intensity ratio values are lower than those of the room temperature values.

Absorption:

Absorption data was used to find out the oscillator strength and hence the integrated absorbance of an electric dipole. Along with this, refractive index of the glass material, reduced matrix elements taken from Carnall et.al.^[10] and the calculated number density (Table 3.1 a-3.1-d) were used to calculate the parameters Ω_2 , Ω_4 and Ω_6 , the well known Judd-Offelt^[6,7] intensity parameters. Calculated Judd-Offelt^[6,7] parameters are tabulated in Tables 3.3a –3.3-d. Due to sample thickness and/or high Eu^{3+} concentrations, it was not always possible to obtain the integrated absorbance from some samples for the transition ${}^7\text{F}_0 \rightarrow {}^5\text{D}_4$, as a result no calculated values of Ω_4 for those samples are available.

The Judd-Offelt^[6,7] intensity parameters have^[22] the following:

a) odd symmetry crystal field terms,

b) radial integrals and

c) perturbation denominators.

The odd crystal field parameter is characteristic of the local distribution or asymmetry in the vicinity around the Eu^{3+} ion. The radial part suggests the admixing of 4f states with 5d and 5g states. The perturbation or the energy denominator indicates the Eu-O covalence^[22].

The Judd-Offelt^[6,7] intensity parameter Ω_2 has the most significant feature in explaining the local structure around the Eu^{3+} ion^[9,23]. Changes in the Ω_2 parameter could be due to one or more of the reasons mentioned above. It has been reported that the increasing value of Ω_2 indicates an increase in the Eu-O covalence and vice versa^[23-25].

Transitions that are largely affected by changes in the environment are called hypersensitive transitions. Selection rules for hypersensitive transitions are $|\Delta J| = 2$ and $|\Delta L| = 2$, $|\Delta S| = 0$ ^[14]. It has been reported that the ${}^7\text{F}_0 \rightarrow {}^5\text{D}_2$ transition of Eu^{3+} ion is site sensitive^[9,14]. For the Eu^{3+} varying series a general trend of increasing Ω_2 parameters was observed with increasing Eu^{3+} concentration. It has also been reported that the larger Ω_2 value results from a larger hypersensitive transition^[9,14,23-25]. Increasing Al showed a small change (increasing) Ω_2 parameters which is associated with increasing Eu-O covalence and Na^+ concentration change did not show any particular trend (Table 3.3-b&c).

The accuracy of Judd-Offelt^[6,7] parameter values is largely dependent on the accuracy of the calculations of the oscillator strength and the calculation of oscillator strength for the ${}^7\text{F}_0 \rightarrow {}^5\text{D}_4$ was error prone. This factor can contribute to spurious values of Ω_4

parameters. Change in Ω_4 parameters corresponds to a change in the viscosity (bulk property) in vitreous material [23] and possibly to a change in the long-range order. A monotonic increase or decrease in the Ω_4 intensity parameter indicates that Ω_4 is not directly related to the ligand symmetry of rare earth ions^[9,23,24].

The Ω_4 parameters for the Eu^{3+} are tabulated in Table 3.3-a which shows the calculated value for two of the samples. For the varying Al concentration (0.000 to 8.775mole percent) Ω_4 parameters increases monotonically.

The Ω_6 parameter increased from 0.5012 to 0.7919 and 0.4602 to 0.824 for the Eu^{3+} series and Al series respectively. For Na^+ varying series Ω_6 parameters did not exhibit much variance. It was stated that Ω_6 parameter is a measure of the force constant of $\text{Eu-O}^{[25]}$ bond and hence Eu-O co-valence^[12,13,25]. According to the theoretical hypothesis by this reference^[25], the intensity parameter Ω_6 should increase with increasing Eu^{3+} or Al^[12] concentration accompanied by a decreasing Ω_2 values. However, the experimental observation by Marcus P. Hellen et. al.^[25] did not match with there theoretical expectations nor does ours.

The values for the Ω_2 parameters (Table-d) were observed for the special sample OPT. For the same 10 mole percent Eu^{3+} concentration, with 2.925 mole% of Al, the value obtained was $6.23 \times 10^{-20} \text{ cm}^2$ whereas when the Al concentration was increased to 13.5 mole%, the Ω_2 parameter value dropped to $3.31 \times 10^{-20} \text{ cm}^2$ i.e. approximately to one half. It indicates that the inhomogeneity was decreased markedly with increasing Al concentration for the same 10 mole% of Eu^{3+} concentration. For these same samples and concentrations the Ω_6 value dropped from 0.790 to 0.605.

Low temperature (-183°C) absorption measurements on the OPT samples allowed calculation of oscillator strengths and hence the Judd-Offelt^[6,7] parameters (with the exception of Ω_4 values as oscillator strengths were unavailable), and these values are tabulated in the Table3.3-d. The low temperature values show that both the parameters Ω_2 and Ω_6 went up for the OPT sample. Increasing Ω_2 indicates a higher co-valence.

CONCLUSION:

Fluorescence and absorption measurements have been conducted for better understanding of local glass structure around Eu^{3+} ion in Eu^{3+} doped aluminosilicate glasses. Room temperature and low temperature (-35°C and -183°C) behavior have been observed for varying concentrations Eu^{3+} , Al and Na^{+} .

Fluorescence integrated intensity ratios of the transitions from ${}^5\text{D}_1$ to ${}^7\text{F}_j$ and from ${}^5\text{D}_2$ to ${}^7\text{F}_j$ have been calculated at room temperature and at -35°C . It has been noted that room temperature ratio values were usually greater than the low temperature ratio values when the numerator is a magnetic dipole allowed transition and the denominator is a forced dipole transition. The magnetic dipole transitions are not very likely to change with the temperature or with the change in the ligand field^[13]. The forced dipole transitions are entirely dependent on the mixing of high energy terms of opposite parity to the $4f^N$ configuration through the static crystal field and/or vibrational contribution^[7]. Since crystal field parameters are not likely to change much with temperature, the decrease in the ratio values can only be due to the vibrational contribution.

Concentration dependence of the fluorescence transitions is rather complicated. For the varying Eu^{3+} ion it was found that the variance in the ratio values of ${}^5\text{D}_1 \rightarrow {}^7\text{F}_0 / {}^5\text{D}_1 \rightarrow {}^7\text{F}_1$ and ${}^5\text{D}_1 \rightarrow {}^7\text{F}_2 / {}^5\text{D}_1 \rightarrow {}^7\text{F}_1$ was small and did not show any particular trend whereas, when varying Al and Na^{+} , clear increasing and decreasing trends of these values have been observed respectively. It suggested that with increasing Al, more radiative decay is forced from the ${}^5\text{D}_1$ states to the ${}^7\text{F}_j$ states, and, at the same time Al decreases the disorder around Eu^{3+} ion thus forcing the forced electric dipole transitions occur less effectively than the magnetic dipole transitions. Where Na^{+} increased disorder in glass structures

around Eu^{3+} ion as more NBO's are created, thus allowing the forced dipole transitions to occur more frequently than the magnetic dipole transitions.

The ${}^5\text{D}_0 \rightarrow {}^7\text{F}_0 / {}^5\text{D}_0 \rightarrow {}^7\text{F}_1$ integrated intensity ratio values did not show any particular trend for the Eu^{3+} varying series but increasing and decreasing values have been observed for the varying Al and Na^+ respectively. The ${}^5\text{D}_0 \rightarrow {}^7\text{F}_0$ transition is a forbidden one by the Judd-Offelt^[6,7] theory in addition to the parity selection rule^[14]. It was suggested that this transition be allowed by J mixing^[14,17-19] can borrow intensity from the ${}^5\text{D}_0 \rightarrow {}^7\text{F}_2$ and ${}^5\text{D}_0 \rightarrow {}^7\text{F}_4$ transitions^[20,21] via J mixing. It can be inferred that increasing Al has profound effect in increasing J mixing while Na^+ has the opposite effect.

The ${}^5\text{D}_0 \rightarrow {}^7\text{F}_2 / {}^5\text{D}_0 \rightarrow {}^7\text{F}_1$ integrated intensity ratio values has an important feature and called asymmetry parameter^[15] since it is a measure of the asymmetry or disorder in the local environment around Eu^{3+} ion^[9,15,23]. It was found to increase with increasing Eu^{3+} . A small increase was observed with increasing Al from 0.000 to 8.775 mole% followed by a decrease for the 14.625 mole% of Al. This suggested that the incorporation of Eu^{3+} ion is effective in increasing the hypersensitivity. The concentration dependant behavior of Na^+ is not quite well understood.

The sharp transition line at 570 nm for the OPT sample was quite stunning. Due to the matching of the energy gap between the ${}^5\text{D}_2$ and ${}^7\text{F}_5$ states, it is suggested that this is a ${}^5\text{D}_2 \rightarrow {}^7\text{F}_5$ transition.

Judd-Offelt intensity parameters have been calculated at room temperature for all the series. The temperature dependence has only been conducted for the sample OPT. The parameter τ_2 has been suggested as a measure of Eu-O co-valence^[9,23,24] and hence a measure of the disorder around Eu^{3+} ion and the hypersensitivity^[9,14,15]. It was observed

that the value increased for increasing Eu^{3+} concentration, increased slightly with increasing Al concentration from 0.000 to 8.775 mole% followed by a decrease for the 14.625 mole%. The values for the Na^+ concentrations did not show any particular trend. As mentioned, the integrated intensity ratio ${}^5\text{D}_0 \rightarrow {}^7\text{F}_2 / {}^5\text{D}_0 \rightarrow {}^7\text{F}_1$ is also a measure of the disorder around Eu^{3+} ion in the glass and also a measure of the hypersensitivity, same trend was expected and observed with the change in the concentrations of Eu^{3+} , Al but Na^+ . For the sample OPT, the τ_2 value at liquid nitrogen temperature increased by a factor of 50% from the room temperature value. This suggests that the intensity parameter τ_2 is largely static^[14].

The intensity parameter τ_6 is a measure of the force constant of the Eu-O bond and an increasing value of τ_6 suggests a decreasing value of the force constant of the Eu-O bond^[25]. It was observed that the value τ_6 increased with increasing Eu^{3+} and Al concentrations. This is in direct contrast to the expected values^[12,25]. The intensity parameter τ_4 is a measure of the bulk properties and hence related to the long range order. In most cases these values were not available.

The temperature dependent behavior for the fluorescence transitions were conducted only at room temperature and at -35°C for the varying Eu^{3+} and Al series and only at room temperature for the varying Na^+ concentrations. For a better understanding of the vibrational contribution to the mixing of states, fluorescent measurements should be performed at different temperatures (above and below room temperature). During the fluorescence ratio calculations, the ${}^5\text{D}_0 \rightarrow {}^7\text{F}_4$ transitions have not been considered. It will be good to study this transition because it has been suggested that the intensity of the

transition ${}^5D_0 \rightarrow {}^7F_0$ is dependent on the J mixing and the ${}^5D_0 \rightarrow {}^7F_2$ and ${}^5D_0 \rightarrow {}^7F_4$ transitions.

Only room temperature absorption measurements have been carried out. Low temperature absorption measurements will be able to determine dominant contribution (static or vibrational) to the hypersensitive transitions. Also, Judd-Offelt^[6,7] parameter calculations from the fluorescence transitions should be done and compared with the parameters obtained from the absorption data.

In the glass samples the alkali concentrations have been changed but no measurements have been performed with varying concentrations of alkaline, which may give better feeling about the local structure around the Eu^{3+} ion. Substitution of alkali (Na^+) by another type of alkali (Li^+ or K^+) will also help determining the effect of alkali on the environment around Eu^{3+} ion.

In addition, samples of different concentrations can also be created especially samples with higher Al concentrations, which are of particular interest because of the sharp transition line observed at 570 nm.

Finally, spontaneous electric dipole emission probabilities can be calculated with these calculated intensity parameters. This then can lead to a calculation of branching ratios and quantum efficiencies, which will be able to give a better insight of the glass local structure around Eu^{3+} ion.

APPENDIX:

Calculation of Judd-Offelt Parameter:

1.0

The electric dipole moment operator P can be written as^[14]

$$P = -eD_q^{(1)}, \text{ where } D_q^{(1)} \text{ is a first rank tensor with components } q=0, \pm 1 \quad (\text{A.1.1})$$

and the oscillator strength for an electric dipole transition is given by

$$P = \chi \left[\frac{8\pi^2 m c \sigma}{h} \right] \left| \langle A | D_q^{(1)} | B \rangle \right|^2, \quad (\text{A.1.2})$$

where the transition is taking place from the state $|A\rangle$ to the state $|B\rangle$. In the above expression (A.1.2), m is electron mass, σ is energy of this particular transition in cm^{-1} and χ is Lorentz field correction, that makes allowance for the refractive index.

Let us consider the initial state $|A\rangle$ as

$|A\rangle = |\alpha J M\rangle$, here M is the projection of J and α stands for all additional quantum numbers, required to uniquely define the state.

The final state $|B\rangle$

$$|B\rangle = |\alpha' J' M'\rangle ;$$

according to the Wigner-Eckerd^[5] theorem, the M dependence of the matrix element of the tensor operator $T_q^{(k)}$ between the states $|A\rangle$ and $|B\rangle$ can be calculated as

$$\langle \alpha J M | T_q^{(k)} | \alpha' J' M' \rangle = (-1)^{J-M} \langle \alpha J || T^{(k)} || \alpha' J' \rangle \begin{pmatrix} J & k & J' \\ -M & q & M' \end{pmatrix} \quad (\text{A.1.3}).$$

The last factor is a 3-j symbol, and the tensor operator within the double bars is called as the reduced matrix element.

2.0

In the rare-earth doped crystals/glasses, the crystal field potential in the static model can be expanded as follows^[6] the crystalline potential as

$$V = \sum_{kq} A_q^{(k)} \sum_i r_i^k V_q^k (i, i) \quad (\text{A.2.1})$$

where r_i is the radial coordinate of the i th electron, $V_q^k (i, i)$ is the q th component of the spherical harmonic of order k and $A_q^{(k)}$ is the crystal field parameter. Now, writing the potential as the sum of the even parity and odd parity terms, the Hamiltonian for the system becomes,

$$H = H_0 + V_{\text{even } k} + V_{\text{odd } k} . \quad (\text{A.2.2})$$

In the free ion approximation, the states of the $4f^N$ configurations are linear combinations of Russel-Saunders states and can be written in the form

$$|f^N \alpha [SL] J\rangle = \sum_{S,L} A(S,L) |f^N \alpha SLJ\rangle . \quad (\text{A.2.3})$$

In this intermediate coupling scheme, S and L are not good quantum numbers and α is introduced for the additional quantum numbers that may be required to define the state uniquely. For convenience, it will be written as $|f^N \psi JM\rangle$. Considering this the ground state, the upper state can be written as, $|f^N \psi' J'M'\rangle$.

The electric dipole operator has odd parity; hence, it vanishes between these states since they have the same parity. The intra f - f transitions, therefore, come into play due to the mixing of $4f^N$ configurations into other configurations of higher energy odd parity terms. This mixing may be accomplished by the odd terms of the static-potential or by the vibrational interaction^[7]. Judd and Ofelt^[6,7] worked independently on this matter, and

they considered that mixing of states is accomplished by the perturbation due to the static potential expansion of odd terms of the crystal field potential,

$$V^{C.F.} = \sum_{t,p} A_{\varphi} D_p^{(t)}, \text{ with } t \text{ odd.} \quad (\text{A.2.4})$$

First order perturbation of the ground state and the upper state by this crystal field invokes the mixing in states of a higher energy opposite parity configuration $|\psi^n\rangle$,

where $|\psi^n\rangle$ can be expressed as

$$|\psi^n\rangle = n! \alpha^n [S^n L^n] J^n M^n.$$

Then the perturbed ground state and the upper states are

$$|A\rangle = |f^N \psi J M\rangle + \sum_k \frac{|\psi^n\rangle \langle \psi^n | V^{C.F.} | f^N \psi J M\rangle}{E(4f^N J) - E(\psi^n)} \quad (\text{A.2.5})$$

and

$$|B\rangle = |f^N \psi' J' M'\rangle + \sum_k \frac{|\psi^n\rangle \langle \psi^n | V^{C.F.} | f^N \psi' J' M'\rangle}{E(4f^N J') - E(\psi^n)}. \quad (\text{A.2.6})$$

k is the quantum number of the excited configuration.

Now the electric dipole transition from ground state to the upper state is allowed, and the strength of the dipole transition is

$D =$

$$\left[e \sum_{k,t,p} A_{\varphi} \left\{ \frac{\langle f^N \psi J M | D_q^{(t)} | \psi^n \rangle \langle \psi^n | D_p^{(t)} | f^N \psi' J' M' \rangle}{E(4f^N J') - E(\psi^n)} + \frac{\langle f^N \psi J M | D_p^{(t)} | \psi^n \rangle \langle \psi^n | D_q^{(t)} | f^N \psi' J' M' \rangle}{E(4f^N J) - E(\psi^n)} \right\} \right]^2 \quad (\text{A.2.7})$$

From tensor calculus, $D_q^{(t)}$ and $D_p^{(t)}$ can be written as $\sum_i r_i (C_q^{(t)})_i$ and $\sum_i r_i (C_p^{(t)})_i$

respectively. Then the first term in the summation sign can be expanded as,

$$A_p \langle f^N \psi JM | \sum_i (C_q^{(i)})_i | \psi^n \rangle \langle \psi^n | \sum_i (C_p^{(i)})_i | f^N \psi' J' M' \rangle \langle 4f | r | nl \rangle \langle nl | r' | 4f \rangle$$

$$\times [E(4f^N J') - E(\psi^n J)]^{-1} .$$

(A.2.8)

Similarly, the second term in the summation can be expanded, and then applying the Wigner-Eckered theorem, 3-j and 6-j symbol, the following equation can be derived^[14]

$$D = \left[e \sum_{p,l,\text{even}\lambda} (-1)^{p+q} A_p [\lambda] \Xi(t, \lambda) \begin{pmatrix} 1 & \lambda & l \\ q & -p-q & p \end{pmatrix} \langle f^N \psi JM | U_{-p-q}^{(\lambda)} | f^N \psi' J' M' \rangle \right]^2 .$$

(A.2.9)

Here the 6-j symbol restricts the value of the λ to be even and less than 6.

And here

$$\Xi(t, \lambda) = 2 \sum (-1)^{l+q} [f] [l] \begin{pmatrix} 1 & \lambda & l \\ f & l & f \end{pmatrix} \langle f || C^{(l)} || l \rangle \langle l || C^{(l)} || f \rangle \langle 4f | r | nl \rangle \langle nl | r' | 4f \rangle \Delta E(\psi^n)^{-1}$$

(A.2.10)

Using the 3-j symbol, in (A.2.9), the matrix element of the tensor operator could be reduced; thus, the strength of an electric dipole becomes

$$P_{E.D.} = \chi \left[\frac{8\pi^2 m c \sigma}{h} \right] \left[\sum_{p,l,\text{even}\lambda} (-1)^{p+q} [\lambda] A_p \begin{pmatrix} 1 & \lambda & l \\ q & -p-q & p \end{pmatrix} \begin{pmatrix} J & \lambda & J' \\ -M & -p-q & M' \end{pmatrix} \Xi(t, \lambda) \langle f^N \psi J || U^{(\lambda)} || f^N \psi' J' \rangle \right]^2 .$$

(A.2.11)

For isotropic light, the 3-j symbol can be replaced by a factor $3^{-1}(2J+1)^{-1}(2l+1)^{-1}$, and finally the strength of an electric dipole becomes

$$P_{E.D.} = \sum_{\lambda=2,4,6} \sigma T_{\lambda} \langle f^N \alpha [SL] J \| U^{(\lambda)} \| f^N \alpha' [S'L'] J' \rangle^2 (2J+1)^{-1} .$$

(A.2.12)

Here,

$$T_{\lambda} = \chi \left[\frac{8\pi^2 mc}{3h} \right] \left[\lambda \sum_{p,t} |A_{\varphi}|^2 \Xi^2(t, \lambda) (2t+1)^{-1} \right] .$$

Since χ varies with wavelength, it is taken out of the summation sign and is not incorporated in the Judd-Offelt parameters. Then

$$P_{E.D.} = \chi \left[\frac{8\pi^2 mc}{3h} \right] \sigma \sum_{\lambda=2,4,6} \Omega_{\lambda} \langle f^N \alpha [SL] J \| U^{(\lambda)} \| f^N \alpha' [S'L'] J' \rangle^2 (2J+1)^{-1} ,$$

(A.2.13)

where

$$\Omega_{\lambda} = \left[\lambda \sum_{p,t} |A_{\varphi}|^2 \Xi^2(t, \lambda) (2t+1)^{-1} \right] , \quad (A.2.14)$$

which are known as the Judd-Offelt intensity parameters.

BIBLIOGRAPHY:

1. Optical spectra of transparent rare earth compounds: Hufner S., Academic Press, New York, 1978.
2. Spectra and energy levels of rare earth ions in crystals: Gerhard Heinrich Dieke, Interscience Publishers, 1968.
3. Van Vleck, J. H.: J. of Chem. Phys. 41 (1937) 67.
4. Dieke, G.H., Advances in Quantum Electronics , Columbia University Press, 1961.
5. Spectroscopic properties of rare earth's: Brian G. Wybourne, Interscience Publishers, 1965.
6. Judd, B. R., Phys. Rev. 127 (1962) 750.
7. Offelt, G. S.: J. of Chem. Phys. 37 (1962) 511.
8. Morgan, H. R., Chock, E.P., Hopewell, W. D., Al-Sayed, M. A., Orbach, R.: J. of Phys. Chem. Solids 85 (1981) 747.
9. Nageno, Y., Takebe, H., Morinaga, K., Izumitani, T.: Journal of Non-Crystalline Solids 169 (1994) 288.
10. Carnall, W. T., Fields, Pr. R., Rajnak, K.: J. of Chem. Phys. 49 (1968) 450.
11. Reisfeld, R., Lieblich, N.: Journal of Phys. Chem. Solids 34 (1973) 1476.
12. Tanabe, S., Hanada, T.: J. of Non-cryst. Solids 196(1996) 101.
13. Tanabe, S.: J. of Non-cryst. Solids 259 (1999) 1.
14. Peacock R. D., Structure & Bonding 22 (1975) 83.
15. Zahir, M. et. al.: Journal of Non-Crystalline Solids, 69 (1985) 221.
16. Lyayne, C. B., Lowdermilk, W. H., Weber, M. J.: Phys. Rev. **B 16** (1977) 10.
17. Cromier, G. et.al.: Phys. Rev. **B 48** (1993) 16290.

18. Tanaka, M. Kushida, T.: Phys. Rev. **B** 52 (1995) 4171.
19. Blaznet B. et.al.: Journal of solid state chemistry 32 (1980) 185.
20. Nishirmura, G., Kushida, T.: Phys. Rev. **B** 37 (1988) 9075.
21. Tanaka M., Nishirmura, G., Kushida, T.: Phys Rev. **B** 49 (1994) 16917.
22. Krupke W. F., IEEE J. of Quantum Electronics 10 (1974) 450.
23. Oomen, E. W. J. L., Van Dongen, A. M. A.: J. of Non-Cryst. Solids 111 (1989) 205.
24. Tanabe, S., Ohyagai, T., Soga N., Hanada, T.: Phys. Rev 45 (1992) 3305.
25. Hellen, M. P., Nigel J. C., Gosnell, T. R., Bruce, A. J.: Phys Rev. **B** 56(1997) 9302.

VITA
ABDUR RAHMAN
Candidate for the Degree of
Master of Science

Thesis: FLUORESCENCE AND ABSORPTION MEASUREMENTS OF EUROPIUM
DOPED ALUMION-SILICATE GLASSES

Major Field: Physics

Biographical Data: Born in Dhaka, Bangladesh, August 16, 1970, the son of Shamsul
Haque and Hosne Haque.

Education: Received Bachelor of Science Degree and Master of Science Degree in
Physics from University of Dhaka, Bangladesh; completed requirements for
the Master of Science Degree at Oklahoma State University, Stillwater,
Oklahoma in July, 2000.